

Horizon 2020 Grant Agreement no: 814523

**Terahertz end-to-end wireless systems supporting ultra-high data
Rate applications**

ThoR

D5.5

**Final Report on Antenna, Propagation and
Channel Models**

Coordinator (EU): Thomas Kürner
 Organisation: Technische Universität Braunschweig

Coordinator (Japan): Tetsuya Kawanshi
 Organisation: Waseda University

Start date of project: 01-Jul-2018

Date of issue: 31-May-2021
 Due date: 30-Apr-2021
 Ref: ThoR_CIT_210408_C_WP5

**Leader in charge of deliverable: Akihiko Hirata
 Chiba Institute of Technology**

Project co-funded by the European Commission within the Horizon 2020 programme and the National Institute of Information and Communications Technology in Japan (NICT)		
Dissemination level		
PU	Public	X
PP	Restricted to other programme participants (including the Commission Services)	
RE	Restricted to a group specified by the consortium (including the Commission Services)	
CO	Confidential, only for members of the consortium (including the Commission Services)	

2. ABBREVIATIONS

AUT	Antenna under Test
BW	Bandwidth
CDF	Cumulative Distribution Function
EDFA	Erbium Doped Optical Fiber Amplifier
EM	Electromagnetic
EO	Electrooptic
FG	Function Generator
FS	Frequency Shifter
FSPL	Free-space Propagation Loss
FWHM	Full Width at Half Maximum
IF	Intermediate Frequency
ITU-R	International Telecommunication Union - Radiocommunication Sector
LD	Laser Diode
LIA	Lock-In Amplifier
LO	Local Oscillator
LOS	Line of Sight
NLOS	No Line of Sight
OBPF	Optical Bandpass Filter
PMF	Polarization Maintaining Fiber
PD	Photodiode
RAU	Remote Antenna Units
RF	Radio Frequency
RSL	Received Signal Level
Rx	Receiver
SNR	Signal-to-Noise Ratio
THz	Terahertz
THz-TDS	Terahertz Time-Domain Spectroscopy
TIA	Transimpedance Amplifier
Tx	Transmitter
UTC-PD	Uni-Traveling-Carrier Photodiode
VNA	Vector Network Analyser

3. Executive summary

It is important to build antenna and propagation models of THz wireless communications in order to evaluate the interference between other services, and to estimate the quality of THz wireless communications. In the ThoR project, we have investigated various researches about antenna and propagation models, and the first results of preliminary antenna, propagation and channel models are summarized as a deliverable D5.2 “Preliminary antenna, propagation and channel models” [3.1].

This deliverable provides the final results of investigations about antenna, propagation and channel models. First, we measured the antenna patterns of a low-gain antenna and a high-gain antenna by using a vector network analyser (VNA) and electro-optic (EO) sensor. We also investigated the near-field to far-field transformation, and showed that the main lobe agrees well between the far-field measurement results and the near-field-to-far-field transformation agrees well.

As for the propagation model, we investigated the effects of wind and diffraction, and found that the probability of gain degradation is significant for the 0.6 m-antenna, however better for the 0.3 m-antenna under the strong wind condition. We also measured the complex dielectric constant of building materials, such as glass, concrete, and etc. by VNA and THz-time-domain spectroscopy (TDS). We used the measurement results of building material dielectric constant for the propagation simulation in metropolitan areas. In the propagation simulation, we investigated the reflection by building materials, and the dependence of the path loss on weather conditions. We conducted path loss investigation to design THz links which offer stable data transmission under various weather conditions, including heavy rain, strong storm, etc., and found that 300GHz THz links can offer over 300m transmission under very severe weather condition, where the transmission data rate would be close to 100Gb/s using QPSK with 51.84GHz bandwidth (BW).

REFERECES.

[3.1] <https://thorproject.eu/wp-content/uploads/2021/02/ThoR-D5.2-Preliminary-antenna-propagation-and-channel-models.pdf>

4. Introduction

The ever-increasing demand for higher data transfer rates in up- and down-link for each device in a cellular network leads to huge aggregated data rates, especially in cities. A fibre connection will probably not be feasible everywhere either for financial or practical reasons like timing issues or problems with the trench work. Existing radio solutions are limited to a few Gigabit-per-second and will hardly be able to cope with the increased traffic. Terahertz (THz) wireless communications, in the frequency range from around 300 GHz to 3 THz, are a very promising solution for ultra-broadband short range backhaul links.

Antenna models and propagation models are important in order to evaluate the communication quality of THz wireless systems, or in order to avoid the interference between backhauls and fronthauls or with other passive services. The parameters of antenna and propagation models described in Recommendation International Telecommunication Union Radiocommunication Sector (ITU-R) are referred in the studies of the communication quality and in the sharing studies. ITU-R defines the antenna pattern models in its recommendation ITU-R F.699 and F.1245. However, these recommendations only cover the frequency range of up to 87 GHz, and there are no recommendations that define the radiation pattern of antennas at a frequency range of over 100 GHz. As for the propagation model, ITU-R P. 1238 covers the frequencies up to 450 GHz, however, other propagation models, such as ITU-R P. 620, P. 1410, and P. 2001, do not exceed 100 GHz. The material models, which are necessary to estimate the reflection/transmission of radio waves, are also proposed in ITU-R Recommendations. ITU-R P. 527 describes the material models of water, soil, and ice up to 1000 GHz. However, other ITU-R Recommendations, such as P. 1238 and P. 2040, are only covering the frequency range up to 100 GHz. Therefore, we have to make a new antenna and propagation model that can be used at the 300-GHz-band.

We evaluated near-field and far-field radiation patterns of various 300-GHz-band antennas using a vector network analyser (VNA) and electro-optic (EO) probe system to develop new antenna models at 300 GHz. Furthermore, we have conducted the trial production of a 300-GHz band transmitter for far-field measurement of high-gain antennas.

As for propagation models, we have conducted various propagation experiments for the construction of propagation models. We also measured the complex dielectric constant of various building materials by using VNA and terahertz time-domain spectroscopy (THz-TDS) and conducted the propagation simulations using the new material models. In addition, we theoretically evaluate the effects of the fluctuation of the beam axis caused by strong wind on the communication quality of 300-GHz-band wireless links.

5. ANTENNA MODEL

5.1. Issues of antenna pattern measurement at 300 GHz

Figure 5.1.1 shows ThoR’s concept. The goal of the ThoR project is to establish 1km THz wireless link with the data rate of more than dozens of Gbps. Besides the V-band and E-band modems, RF front ends and THz amplifiers, high-gain antennas are key enabling components to achieve this goal. The Cassegrain antenna is one of the promising candidates for such high-gain antennas. Figure 5.1.1 also shows an example of a Cassegrain antenna for the 300-GHz band. The diameter of this Cassegrain antenna is 152 mm and its antenna gain is 48 dBi. The characterization of the antenna is important to evaluate the interference between other services, and to estimate the quality of THz wireless communications.

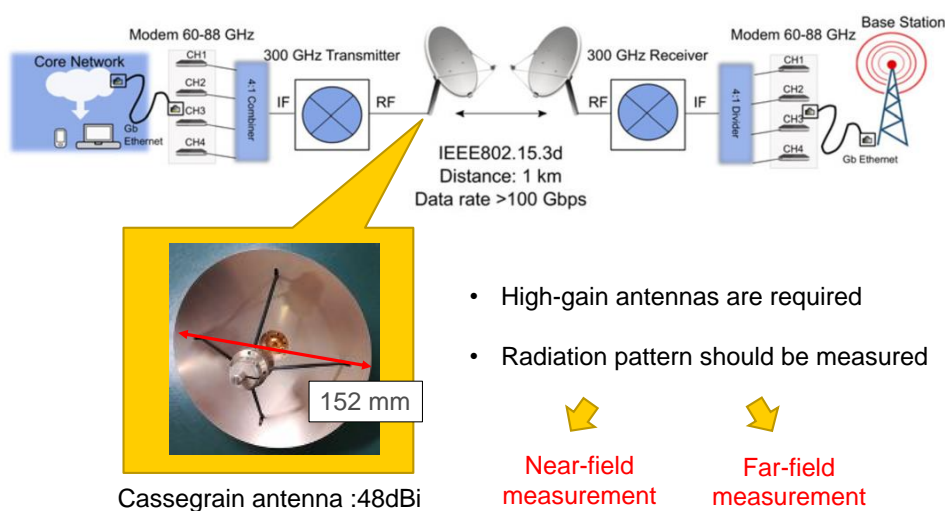


Figure 5.1.1: Reactive near-field, radiative near-field, and far-field region.

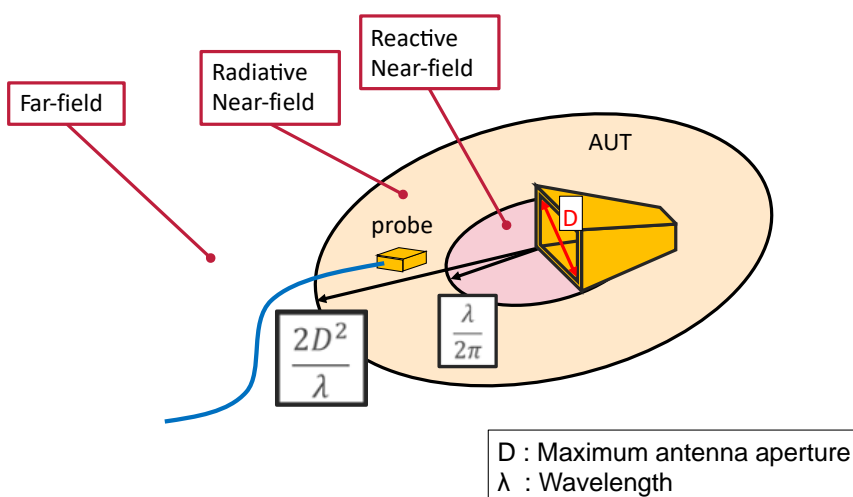


Figure 5.1.2: Schematic illustration of the reactive near-field, radiative near-field, and far-field region.

As shown in Figure 5.1.2, the field emitted from the antenna can be divided into three categories: reactive near-field, radiative near-field, and far-field. The far-field measurement is a popular method for radiation pattern (far-field pattern) characterization. For the far-field measurements, the probe needs to be placed in the far-field region.

It is difficult to measure the accurate radiation pattern of high gain antennas at 300 GHz, since the antenna pattern should be measured at the far field, and the far-field boundary of the high-gain antenna with a gain of about 50 dBi is estimated to be dozens of meters.

In case of the reflector antenna, the boundary of far field (r) is described as

$$r = \frac{2D^2}{\lambda} \quad \cdot \cdot \cdot \text{Eq. 5.1.1}$$

D is the diameter of the antenna aperture, and λ is the wavelength. In case the antenna gain is 45 dBi (antenna diameter is 0.15 m) and the frequency is 300 GHz, the boundary of far field (r) is 45 m. However, it is difficult to measure the high gain antenna radiation pattern over a distance of dozens of meters in an anechoic chamber.

Moreover, the free space transmission loss becomes larger than 100 dB over this distance. In case the transmission characteristics is 45 m, the free-space propagation loss (FSPL) is described as

$$\text{FSPL} = \left(\frac{4\pi r}{\lambda}\right)^2 = 115 \text{ dB} \quad \cdot \cdot \cdot \text{Eq. 5.1.2}$$

Therefore, the received power is quite small. Moreover, the ratio of the main lobe over the side lobe of the high gain antenna is over 70 dB in case of a high-gain antenna. Hence, the required minimum sensitivity of the receiver (Rx) should be very high. However, it is difficult to achieve such a high sensitivity at 300 GHz.

On the other hand, near-field measurement technique provides several advantages over the far-field measurement. The distance between the probe and the AUT can be shortened, which makes the measurement system very compact. For the frequency of 300 GHz, the distance which divides the reactive near-field region and radiative near-field region is about 0.16 mm. Several millimeters of distance between the antenna and the probe are enough for the near-field measurement. However, the probe placed in the near-field region might disturb the field to be measured. Mutual coupling between the antenna under test and the probe might occur. Also, scattering from the probe will be a serious problem, reducing the accuracy of the measurements. Special attention should be needed to minimize the disturbance which is introduced by the probe itself.

In this section, we described the measurement results of far-field antenna pattern by VNA and 300-GHz-band Tx/Rx in Sec. 5.2 and 5.3, respectively. We also measured the near-field antenna pattern by VNA and EO probe system and converted it to far-field antenna pattern in Sec. 5.4 and 5.5, respectively. In Sec. 5.6, we compared the far-field antenna pattern measured by different method, and discussed the accuracy of each methods. In Sec. 5.7, we compared the far-field antenna patterns with the ITU-R models.

5.2. Far-field antenna pattern measurement at 300 GHz by VNA

Figure 5.2.1 shows the photograph of the measurement setup for the far-field radiation pattern of low gain antenna. The transmission distance is 0.5 m, and the azimuth angle and elevation angle of Rx was rotated. The measurement was conducted in an anechoic chamber. We used an orthogonal horn antenna with a gain of 25 dBi as a low gain antenna. The photograph of the orthogonal horn antenna is shown in Fig. 5.2.2.

Figure 5.2.3 shows the measured magnitude of the far-field radiation pattern. The half beam width of the antenna was about 1.9 degree.



Figure 5.2.1: Measurement setup for the characterization of the far-field radiation pattern

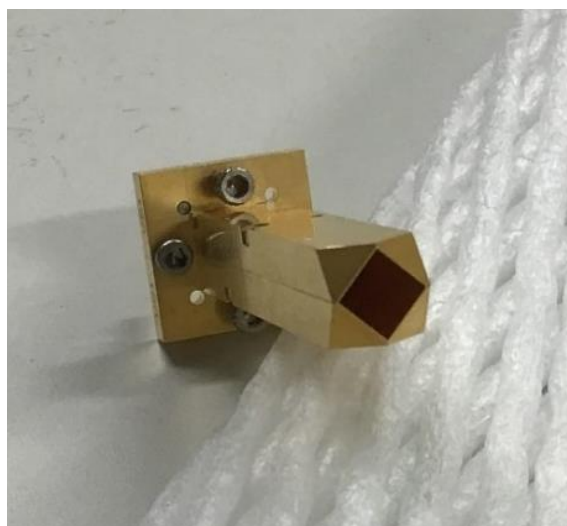


Figure 5.2.2: Photograph of the 300-GHz-band orthogonal horn antenna.

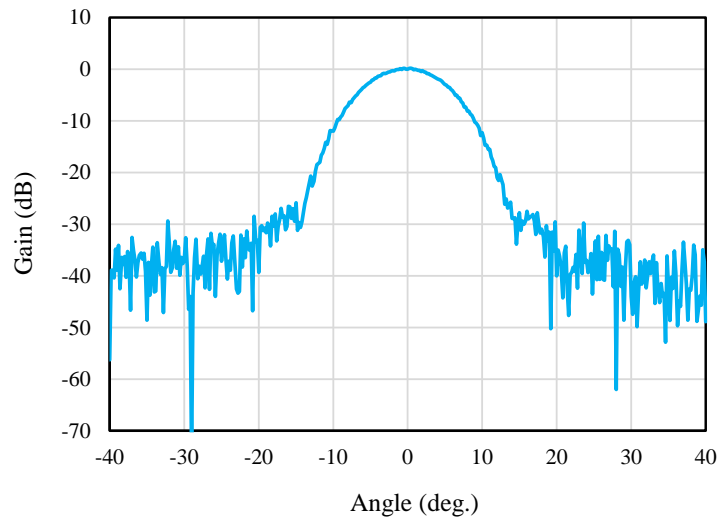


Figure 5.2.3: The far-field pattern measured by the setup shown in Fig. 5.2.1

5.3. Far-field measurement by Tx/Rx

We have conducted the trail production of a 300-GHz band transmitter for the far-field antenna pattern measurement of high-gain antenna. Figure 5.3.1 shows a schematic of the transmitter and receiver system. The transmitter consists of a frequency-multiplier chain with a multiplication factor of 9. The carrier frequency of the transmitter is 293.4 GHz, and the output power is 1.2 mW. The transmitter employs two antennas, a Cassegrain antenna with a gain of 45 dBi, and an orthogonal horn with 25 dBi.

The receiver employs a sub-harmonic mixer. The output IF signal is 24 MHz. The magnitude of the output IF signal was measured by a spectrum analyser.

We obtained an experimental radio station licence from Kanto General Communication Bureau on 20th November 2020. The photograph of the transmitter is shown in Fig. 5.3.2.

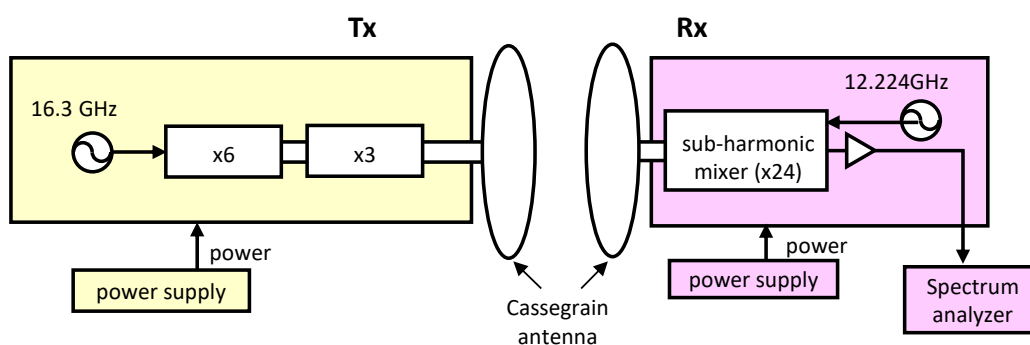


Figure 5.3.1: Schematic of the 300-GHz-band transmitter and receiver system.



Figure 5.3.2: Photograph of the experimental setup of antenna pattern measurement.

We evaluated the radiation pattern of the low-gain antenna by using the Tx and Rx described above, and compared these results with the radiation pattern measured by the VNA. We measured the radiation pattern of the orthogonal horn antenna with a gain of 25 dBi shown in Sec. 5.2. The schematic and the photograph of the experimental setup is shown in Fig. 5.3.3 and Fig. 5.3.4, respectively. The Tx was rotated by a rotator, and the motion of the rotator was controlled by a PC. The intermediate frequency (IF) magnitude was measured by a spectrum analyser, and the rotator angle and the magnitude of the IF signal was recorded synchronously.

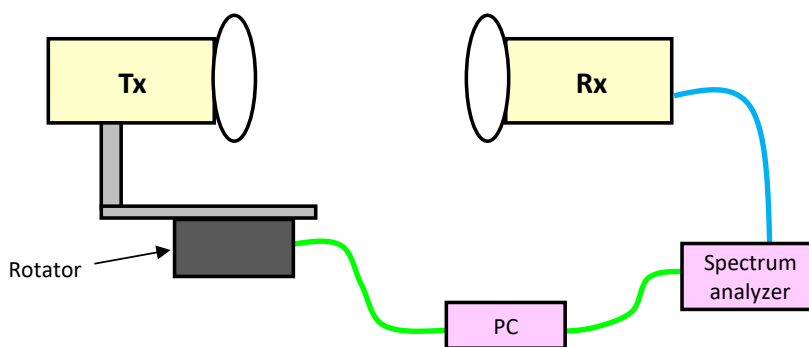


Figure 5.3.3: Experimental setup for the measurement of far-field radiation pattern



Figure 5.3.4: Photograph for the measurement of far-field radiation pattern

Figure 5.3.5 shows the radiation pattern of the orthogonal horn antenna measured by VNA and the Tx/Rx system shown in Fig. 5.3.3. The transmission distance was 0.5m for both systems. The main lobe pattern measured by VNA and the Tx/Rx system agrees well. Moreover, the dynamic range of the Tx/Rx measurement system is over 30 dB larger than that of VNA system. These results indicate the Tx/Rx measurement system can measure the radiation pattern with very good accuracy, and can achieve a large dynamic range.

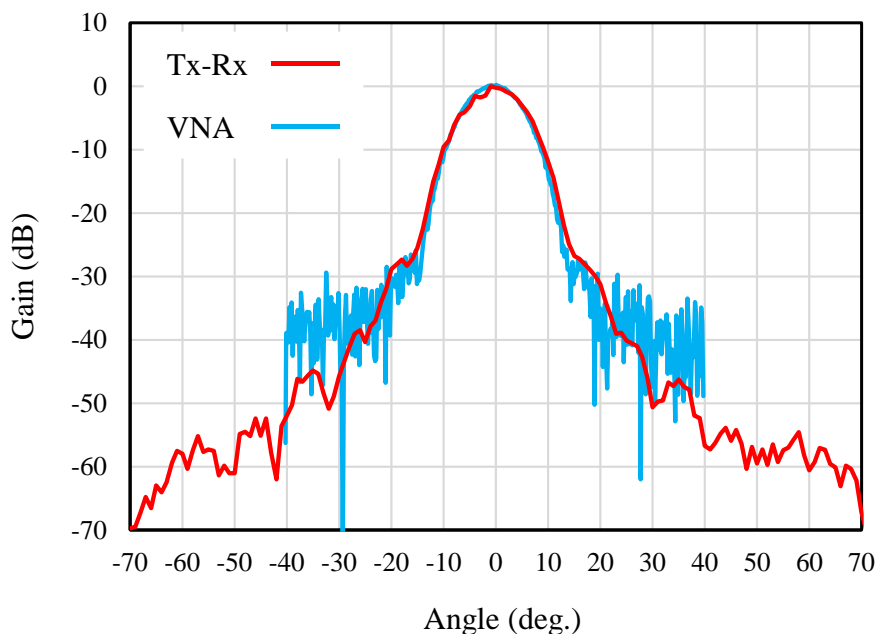


Figure 5.3.5: Radiation pattern of the orthogonal horn antenna measured by VNA and Tx/Rx system

We are now measuring the far-field radiation pattern of the high-gain antenna. Figure 5.3.6 shows the photograph of the far-field radiation pattern measurement. The transmission distance was 50 m. Figure 5.3.7 shows the far-field radiation pattern of the Cassegrain antenna with a gain of 45 dBi and with a diameter of 150 mm. These results indicate that the Tx/Rx system can be applied for the far-field characterization of high-gain antennas.



Figure 5.3.6: Photograph of the far-field radiation pattern measurement

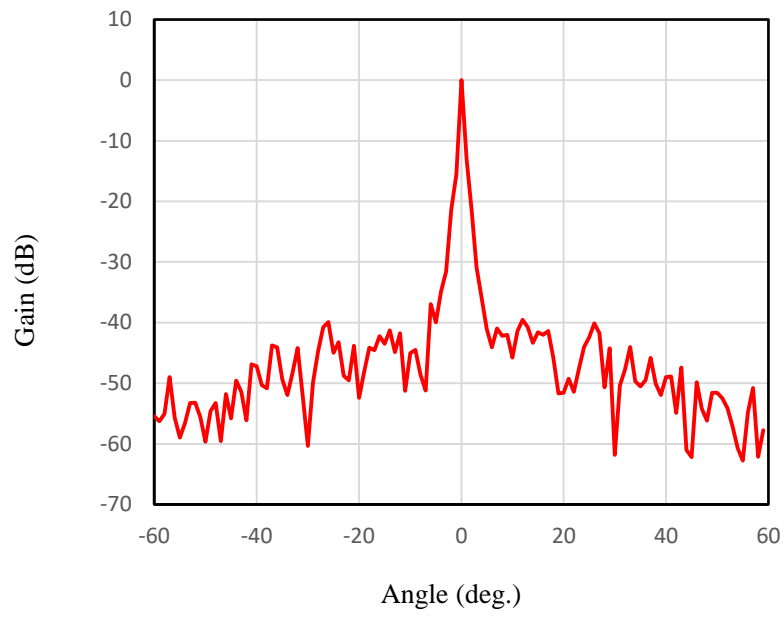


Figure 5.3.7: Radiation pattern of the Cassegrain antenna.

5.4. Near field antenna pattern measurement by VNA

Figure 5.4.1 shows the photographs of the measurement setups for the characterization of the near-field radiation pattern. The transmission distance between the Tx antenna and Rx antenna is 2 mm. Both of Tx antenna and Rx antenna employ the orthogonal horn antenna described in Sec. 5.2 and 5.3. In case of the near-field measurement, planar scanning was employed by using a X-Y scanner. The interval of the scanning step is 0.46 mm, and the scanning area is 19.32mm X 19.32 mm.

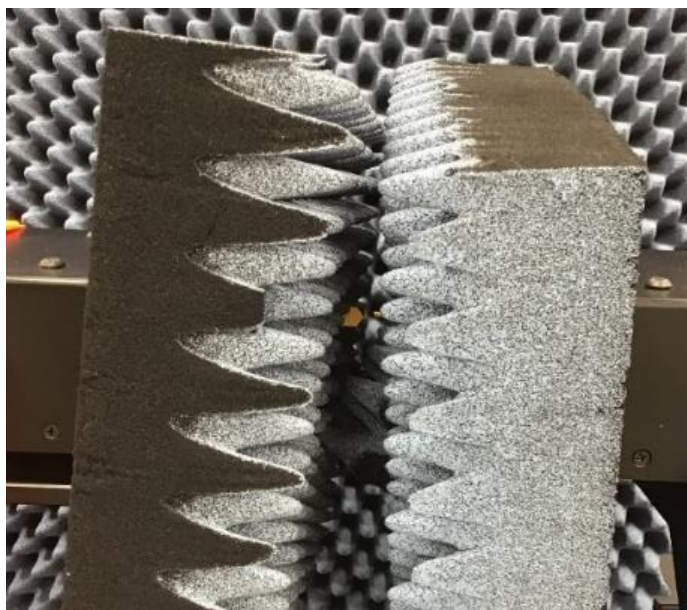


Figure 5.4.1: Measurement setup for the Characterization of the near-field radiation pattern

Figure 5.4.2 shows the measured magnitude of the near-field radiation pattern. Figure 5.4.3 shows the far-field radiation pattern of the orthogonal horn antenna converted from the measured near-field radiation pattern shown in Fig. 5.4.2. The far-field pattern measured by the setup depicted in Fig. 5.3.4 is also shown. The main lobe agrees well, however, we have to improve the side lobe region by introducing the cylindrical scanning system.

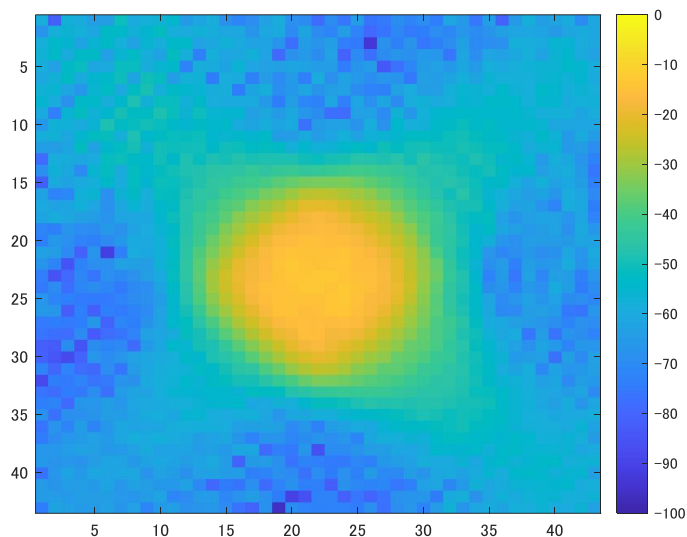


Figure 5.4.2: Measured magnitude of the near-field radiation pattern.

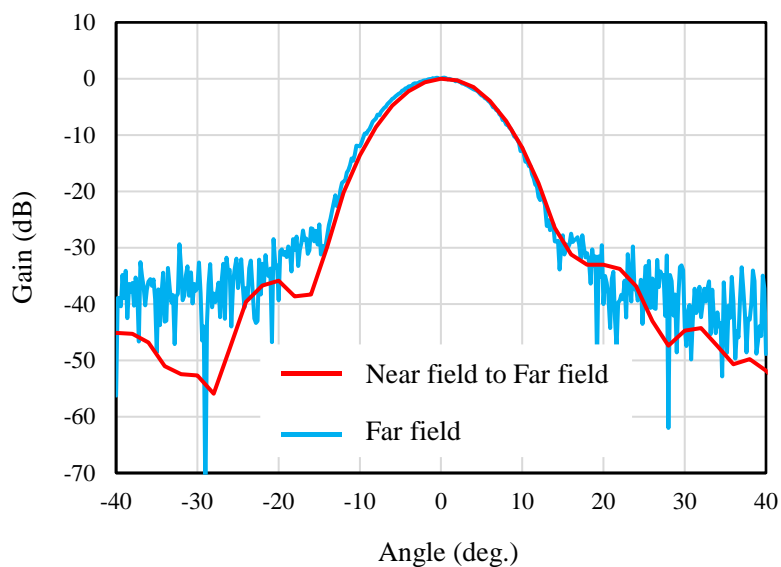


Figure 5.4.3: Far-field radiation pattern of the orthogonal horn antenna converted from the measured near-field radiation pattern. The far-field pattern measured by the setup shown in Fig. 5.3.4 is also shown.

5.5 Near field antenna pattern measurement by EO

In this section, the near-field measurement based on an electro-optic (EO) sensing system and its application to far-field characterization will be discussed.

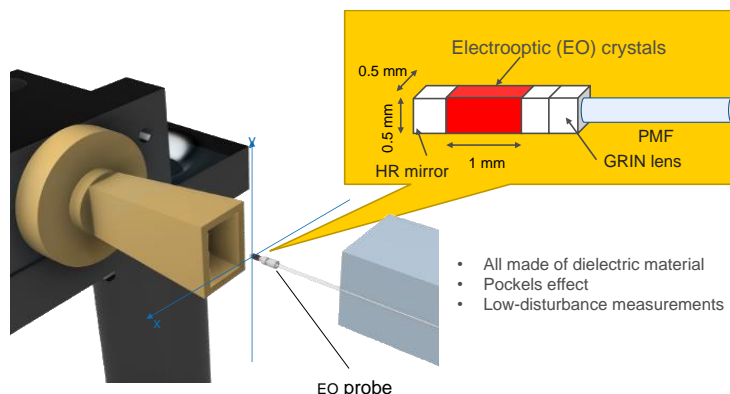


Figure 5.5.1: Electro-optic (EO) probe and its placement for the near-field measurement.

To minimize the disturbance, we use a dielectric probe, instead of the conventional probe antenna. Figure 5.5.1 shows the schematic of the EO probe. The EO probe consists of an EO crystal, GRIN lens and polarization maintaining optical fiber. There are no metallic elements on the EO crystal which minimizes the scattering by the probe head. Hence, the optical fiber drastically reduces the scattering compared with a conventional probe antenna in which metallic cable is used. The dimensions of the probe head are 0.5mm, 0.5 mm and 1 mm.

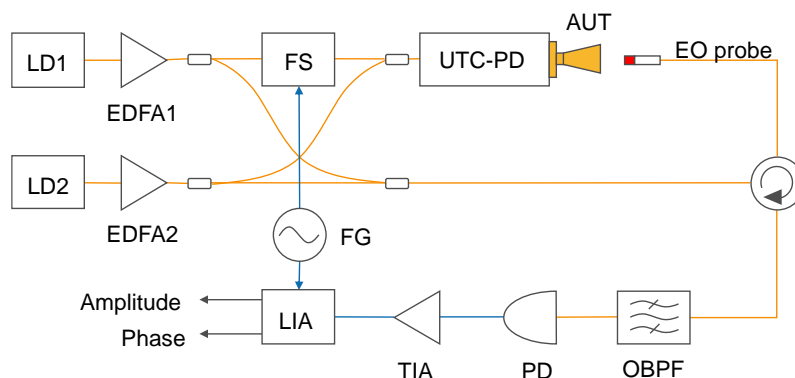


Figure 5.5.2: Near-field measurement system based on the self-heterodyne technique. AUT: antenna under test, UTC-PD: Uni-traveling-carrier photodiode, FS: frequency shifter, LD: laser diode, EDFA: Erbium doped optical fiber amplifier, OBPF: optical bandpass filter, PD: photodiode, TIA: transimpedance amplifier, LIA: lock-in amplifier, FG: function generator.

Figure 5.5.2 shows the near-field measurement system based on the self-heterodyne technique. The system generates the radio frequency (RF) signal and local oscillator (LO) signal to measure the amplitude and phase distribution of a near-field. The RF and LO signals are generated using two free-running 1550 nm laser diodes (LDs). Although the frequency of the RF signal fluctuates, not only the amplitude but also the phase distribution is visualized. The frequencies of the LDs are set as f_1 and f_2 ($f_2 > f_1$) and combined using polarization maintaining fiber (PMF) couplers to produce a beat note at a frequency of $f_{THz} = f_2 - f_1 - f_s$ for THz wave generation (RF signal generation). Here, an EO frequency shifter is used to shift the frequency of the LD1 (f_1) by f_s (typically 100 kHz to 10

MHz) for self-heterodyne detection. A high-speed PD such as a uni-travelling-carrier photodiode (UTC-PD) can be used as an O/E converter. For the LO signal, a beat note is used as a probe beam for the non-polarimetric EO frequency down-conversion. The intermediate frequency (IF) signal is amplified by the transimpedance amplifier (TIA) and supplied to the lock-in amplifier. The measured amplitude and phase data are acquired by a personal computer.

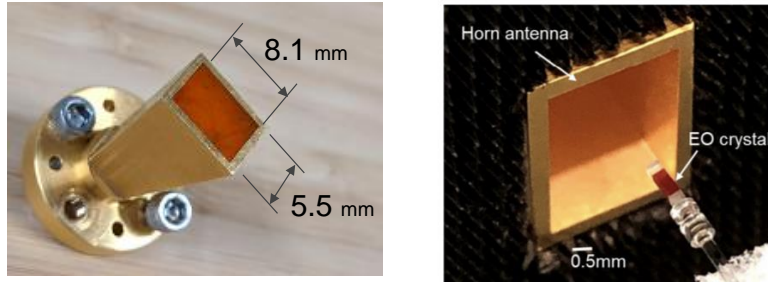


Figure 5.5.3: Rectangular horn antenna as an antenna under test.

To validate the far-field characterization based on the near-field measurement, we employed a standard rectangular-type horn antenna (WR-3.4) as a test sample. We calculated the far-field pattern using measured near-field distribution and compared it with the results obtained by conventional far-field measurements. Figure 5.5.3 shows the AUT. The antenna aperture size of the AUT was 8.1 mm X 5.5 mm. The black part in the photograph is the electromagnetic wave absorber.

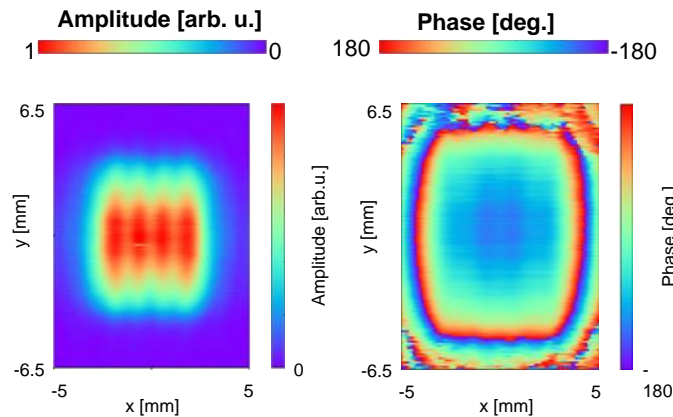


Figure 5.5.4: Measured amplitude and phase distribution of the near-field.

Figure 5.5.4 shows the measured amplitude and phase distribution of the near-field. The frequency of the RF signal was 288 GHz. The measured surface was at $Z = 2$ mm from the antenna surface. The EO probe was moved by 0.1 mm pitch. The time constant of the lock-in detection was 100 ms. The maximum signal-to-noise ratio (SNR) was about 45 dB.

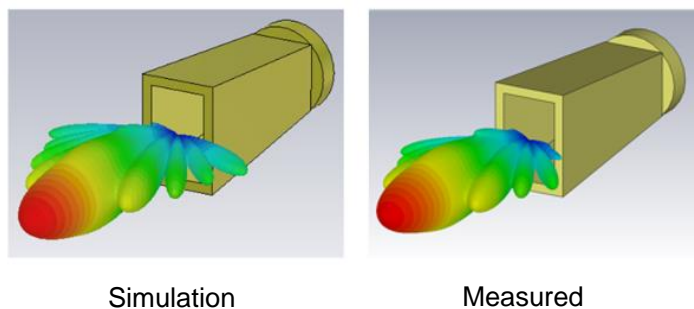


Figure 5.5.5: Far-field pattern calculated from the measured near-field distribution.

The far-field pattern was calculated based on the planner near-to-far field transformation. The simulated results were conducted based on the finite integration technique. The results agreed well with each other except for the third and fourth sidelobe level.

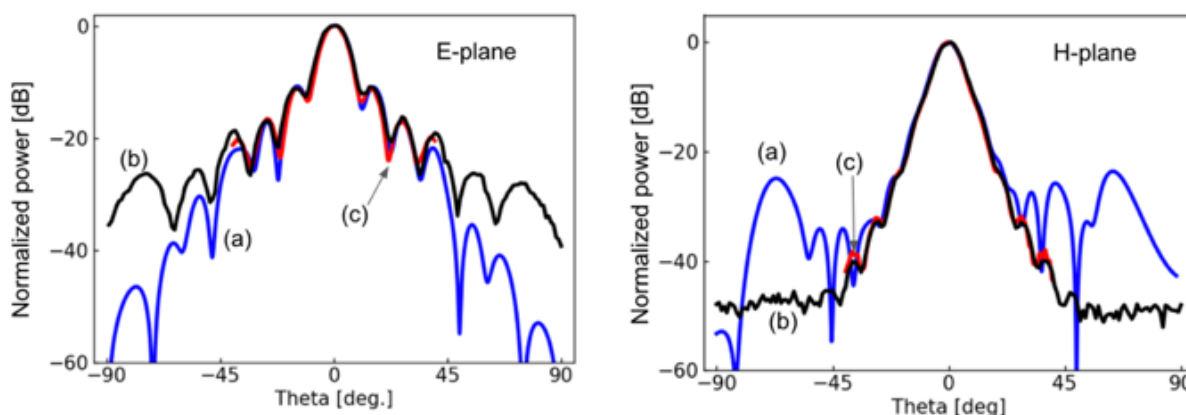


Figure 5.5.6: One dimensional far-field pattern on the E-plane and H-plane. (a) Calculated results from the measured near-field distribution, (b) results obtained by conventional far-field measurement with spherical scanning, (c) results obtained by conventional far-field measurement with planar scanning.

Figure 5.5.6 shows one dimensional far-field pattern on the E-plane and H-plane. Lines (a), (b) and (c) correspond to the calculated result from the measured near-field distribution, the result obtained by conventional far-field measurement with spherical scanning, and the result obtained by conventional far-field measurement with planar scanning, respectively. The measured area of the conventional far-field measurement with planar scanning is limited to -45 deg. to 45 deg. The obtained results agreed well with each other in both planes. Discrepancies between the results based on the near-field measurement (line (a)) and the results obtained by the conventional far-field measurement with spherical scanning (line (b)) are due to the limited measured area of the near-field measurement. To improve the accuracy at the higher spatial frequency region, enlargement of the measurement area is required. This can also be solved by changing the scanning method of the near-field measurement from planer type to cylindrical or spherical type.

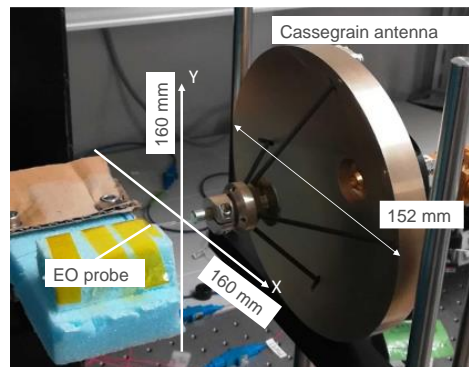


Figure 5.5.7: Cassegrain antenna as an AUT.

Next, we measured the near-field of a Cassegrain antenna and calculated the far-field pattern. Figure 5.5.7 shows the Cassegrain antenna as an AUT. This antenna is different with the Cassegrain antenna shown in Sec. 5.3. The diameter of the AUT is $D=152$ mm and the designed antenna gain is 48 dBi.

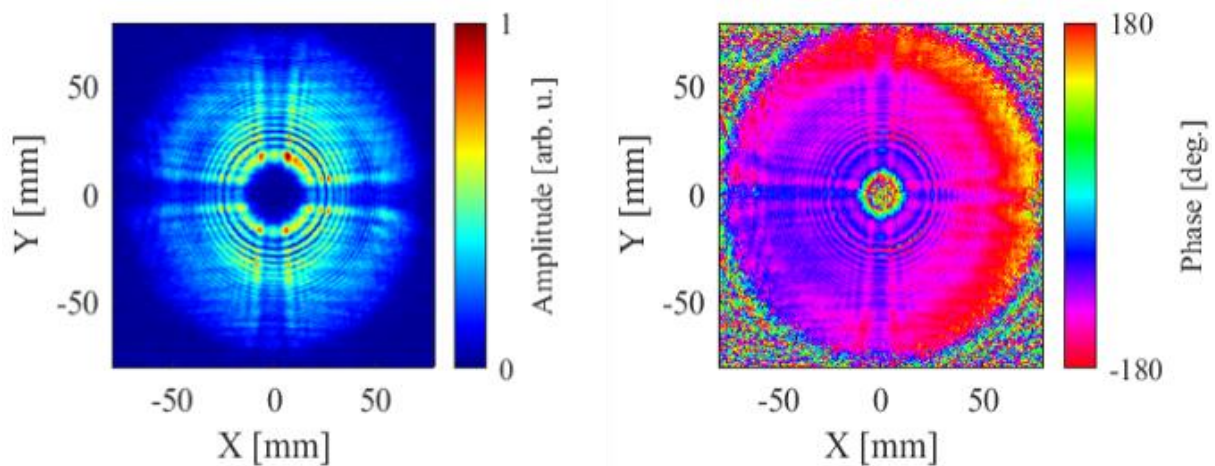


Figure 5.5.8: Measured near-field distribution of the Cassegrain antenna.

Figure 5.5.8 shows the measured near-field distribution. The maximum SNR of this measurement was 25 dB. The theoretically derived standard deviation of the phase measurement limited by the SNR of the measurement can be calculated as 6.4 deg. Although the convex secondary reflector and support elements of the Cassegrain antenna disturb not only the amplitude distribution but also the phase distribution, the overall phase distribution is flat. However, In the phase distribution, there is a little phase tilt. The phase tilt is due to the antenna miss alignment relative to the probe movement.

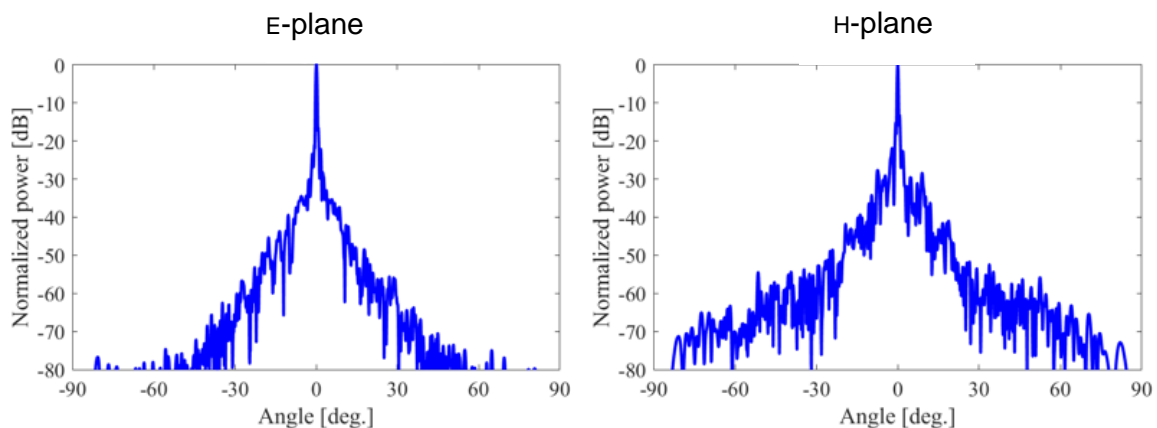


Figure 5.5.9: Calculated far-field pattern of the Cassegrain antenna.

To evaluate the radiation pattern of the Cassegrain antenna, we calculated far-field pattern from the measured near-field distribution. Figure 5.5.9 shows the calculated far-field pattern in the E-plane and H-plane. The full width at half maximum (FWHM) of the radiated beam was 0.46 deg. and 0.40 deg. for E-plane and H-plane, respectively.

5.6 Comparison of antenna pattern measurements

We measured the antenna patterns of low-gain antennas and a high-gain antenna by using a vector network analyser (VNA) and an electro-optic (EO) sensor. We measured the far-field radiation patterns of low gain antennas, such as a horn antenna, in an anechoic chamber by using the VNA. We also measured the near-field pattern of the low-gain antenna by VNA and EO sensors, and the near-field pattern results were transformed to the far-field pattern. The main lobe of the radiation pattern agrees well between the far-field measurement results by VNA and the near-field-to-far-field transformation results measured by VNA and EO sensor.

Discrepancies between the results based on the near-field measurement and the results obtained by the conventional far-field measurement with spherical scanning are due to the limited measured area of the near-field measurement. To improve the accuracy at the higher spatial frequency region, enlargement of the measurement area is required. This can also be solved by changing the scanning method of the near-field measurement from planer type to cylindrical or spherical type.

We also measured the near-field pattern of high-gain antenna (Cassegrain antenna) by EO sensor and transformed it to far-field pattern. The maximum SNR of this measurement was 25 dB. The theoretically derived standard deviation of the phase measurement limited by the SNR of the measurement can be calculated as 6.4 deg. Although the convex secondary reflector and support elements of the Cassegrain antenna disturb not only the amplitude distribution but also the phase distribution, the overall phase distribution is flat.

5.7 Comparison of far-field antenna pattern with ITU-R models

In the Recommendation ITU-R, the far-field radiation pattern of the millimetre-wave reflector antenna is described in Recommendations ITU-R F. 699 and F. 1245.

In ITU-R F. 699, in cases where the ratio between the antenna diameter and the wavelength is greater than 100, the following equations should be used for frequencies in the range 70 GHz to 86 GHz,

$$G(\varphi) = G_{max} - 2.5 \times 10^{-3} \left(\frac{D}{\lambda} \varphi \right)^2 \quad \text{for } 0^\circ < \varphi < \varphi_m$$

$$G(\varphi) = G_1 \quad \text{for } \varphi_m \leq \varphi < \varphi_r$$

$$G(\varphi) = 32 - 25 \log \varphi \quad \text{for } \varphi_r \leq \varphi < 120^\circ$$

$$G(\varphi) = -20 \quad \text{for } 120^\circ \leq \varphi \leq 180^\circ$$

where:

$G(\varphi)$: gain relative to an isotropic antenna (dBi)

φ : off-axis angle (degrees)

D : antenna diameter }
 λ : wavelength } expressed in the same units

$$G_1: \text{ gain of the first side-lobe} = 2 + 15 \log \frac{D}{\lambda} \quad (\text{dBi})$$

$$\varphi_m = \frac{20\lambda}{D} \sqrt{G_{max} - G_1} \quad \text{degrees}$$

$$\varphi_r = 15.85 \left(\frac{D}{\lambda} \right)^{-0.6} \quad \text{degrees}$$

In ITU-R F. 1245, in cases where the ratio between the antenna diameter and the wavelength is greater than 100 ($D/\lambda > 100$), the following equation should be used for frequencies in the range 70 GHz to 86 GHz, the antenna gain G (dBi):

$$G(\varphi) = G_{max} - 2.5 \times 10^{-3} \left(\frac{D}{\lambda} \varphi \right)^2 \quad \text{for } 0^\circ < \varphi < \varphi_m$$

$$G(\varphi) = G_1 \quad \text{for } \varphi_m \leq \varphi < \max(\varphi_m, \varphi_r)$$

$$G(\varphi) = 29 - 25 \log \varphi \quad \text{for } \max(\varphi_m, \varphi_r) \leq \varphi < 120^\circ$$

$$G(\varphi) = -23 \quad \text{for } 120^\circ \leq \varphi \leq 180^\circ$$

where:

G_{max} : maximum antenna gain (dBi) (see Note 2)

$G(\varphi)$: gain (dBi) relative to an isotropic antenna

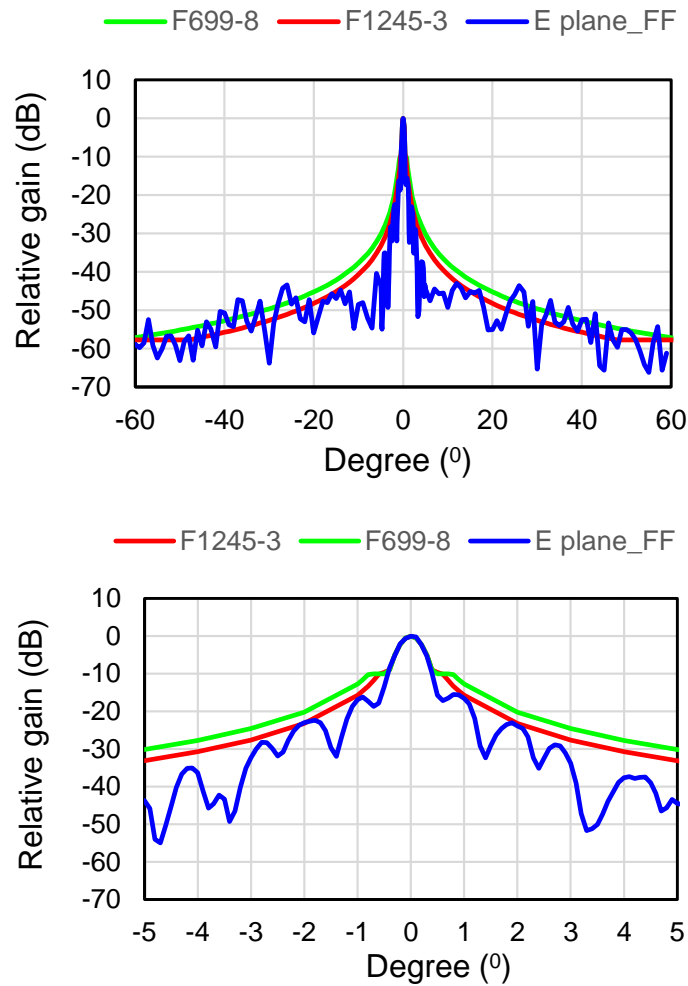
φ : off-axis angle (degrees)

D : antenna diameter }
 λ : wavelength } expressed in the same unit

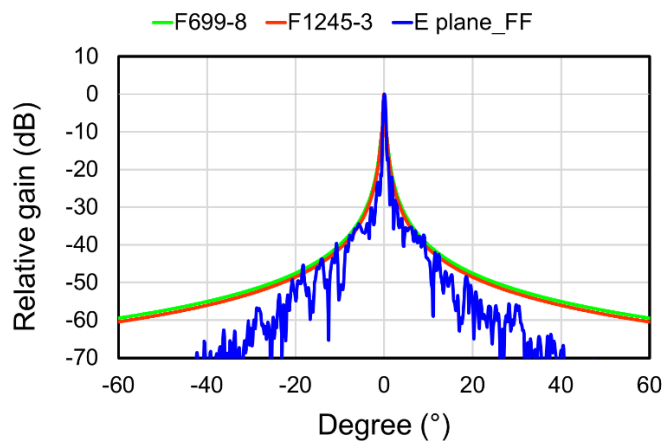
$$\begin{aligned}
 G_1: & \text{ gain of the first side lobe} \\
 = & 2 + 15 \log (D/\lambda) \\
 \varphi_m & = \frac{20 \lambda}{D} \sqrt{G_{max} - G_1} && \text{degrees} \\
 \varphi_r & = 12.02 (D/\lambda)^{-0.6} && \text{degrees}
 \end{aligned}$$

We compared these ITU-R models with the measured radiation patterns of Cassegrain antenna.

Figure 5.7.1 shows the measured far-field pattern of the Cassegrain antenna shown in Fig. 5.3.7 and Fig. 5.5.9. The antenna pattern described in the Recommendation ITU-Rs are overlapped. The main lobe of the measured antenna pattern agrees well with the ITU-R models. The side lobes of the measured radiation pattern also agree with the ITU-R models. However, the side lobe of the measurement results become a few dB larger than the ITU-R models at several degrees.



(a)



(b)

Figure 5.7.1: Radiation pattern of the Cassegrain antenna and ITU-R models. (a) measured far-field patterns, (b) measured near-field pattern by the EO and converted to far field pattern (Fig. 5.5.9).

6. PROPAGATION MODEL

6.1. Introduction to the propagation models used ThoR

In contrast to the sub-6 GHz, propagating waves at 300 GHz frequency bands show different propagation characteristics. The ray is more directive as well as more vulnerable against interactions with objects (e.g., transmission, reflection, diffusion), because THz wireless links employ high-gain antenna in order to achieve sufficient link distance. Besides, the atmospheric conditions strongly affect the additional energy loss of propagating rays at the frequency of 300 GHz. Therefore, presenting a propagation model that appropriates to the 300 GHz carrier frequency is an initial objective to match the simulation results with the results of radio wave propagation in the real environment.

A propagation model that fits for sub-THz frequency bands is suggested in [6.1.1] which additionally considers the atmospheric conditions such as rain. The proposed model already incorporates the prominent elements which have great influence on the energy loss. Nevertheless, it does not cover the impact of antenna misalignment caused by wind which induces an additional power degradation of the received signal. Therefore, the propagation model used in ThoR contains both of the atmospheric conditions as well as the impact of wind and it is

$$\frac{a_{pl}}{dB} = 20 \cdot \log_{10} \frac{d}{km} + 20 \cdot \log_{10} \frac{f}{GHz} + 92.45 + (\gamma_{at} + \gamma_r + \gamma_{cl}) \cdot \frac{d}{km} + \gamma_w. \quad \cdot \cdot \cdot \text{Eq. 6.1.1}$$

The given model compromises fair predictions of the point-to-point propagation loss by including the atmospheric factors which affect the significant attenuation on the propagating rays. Here, γ_{at} refers to the additional attenuation caused by the oxygen molecules and water vapours which are contained in air. The mathematical calculation method of γ_{at} is provided in [6.1.2] and elaborates to predict the specific attenuation at frequencies up to 1000 GHz under any value of air pressure, temperature and water vapour content (humidity). The component of γ_r refers to the additional attenuation induced by rain. [6.1.3] recommends the mathematical equation to obtain the specific attenuation using the rain rate (mm/h). The component of γ_{cl} refers to the additional attenuation caused by small droplets inside of clouds and fog. The mathematical model is based on the Rayleigh scattering effects and provided in [6.1.4]. It facilitates to predict the attenuation considering the quantity of liquid water density in fog. The component of γ_w refers to the power degradation of the received signal which is caused by wind which arises the misalignment of antenna pointing vectors. The mathematical model of the antenna's inclination angle is described in detail further in Section 6.2.

The given propagation model is integrated in the in-house developed mobile network simulator (SiMoNe) [6.1.5]. Each attributes of additional attenuation components are modularized. Therefore, the impact of a single component can be independently identified. So the extension of given propagation model can be easily completed by adding mathematical equations of extra elements.

The specific attenuation of each atmospheric component (γ_{at} , γ_r and γ_{cl}) is separately computed and the values are directly mapped over the ray-tracing results which is generated based on the free space propagation loss (FSPL) while the integration of the impact of wind on the power degradation (γ_w) is accomplished in the following steps

1. calculate the inclination angles of the antennas used in the scenario
2. change the positions and pointing vectors of the antenna based on the inclination angles
3. map the radiation pattern of the antennas over the positions and the pointing vectors
4. compute the actual channel gain of the antenna by applying bilinear interpolation
5. map the value of the resulted channel gain over ray-tracing results

REFERECES

- [6.1.1] A. Fricke, "TG3d Channel Modelling Document", IEEE P802.15 Working Group for Wireless Personal Area Networks (WPANs), March, 2016.
- [6.1.2] ITU-R P.676-12, "Attenuation by atmospheric gases and related effects", August, 2019.
- [6.1.3] ITU-R P.838-3, "Specific attenuation model for rain for use in prediction methods", March, 2005.
- [6.1.4] ITU-R P.840-8, "Attenuation due to clouds and fog", August, 2019.
- [6.1.5] D. M. Rose, J. Baumgarten, S. Hahn and T. Kurner, "SiMoNe - Simulator for Mobile Networks: System-Level Simulations in the Context of Realistic Scenarios," 2015 IEEE 81st Vehicular Technology Conference (VTC Spring), Glasgow, UK, 2015, pp. 1-7, doi: 10.1109/VTCSpring.2015.7146084.

6.2. Modelling of wind effects

The higher frequency link like terahertz link has very narrow beam width, because THz wireless links employ high-gain antenna in order to achieve sufficient link distance. Therefore, the received signal level (RSL) is influenced easily by antenna fluctuation due to strong wind. Figure 6.2.1. depicts an example of measured data in E-band (85.5 GHz), showing strong correlation between the wind speed and the RSL. Hence, it is important to consider the wind effects on the terahertz link in order to estimate the link performance with high reliability.

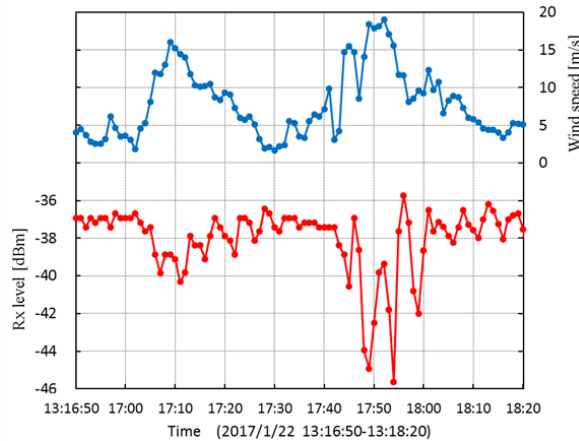


Figure 6.2.1. Example of relationship between wind speed and RSL

In this section, we analyse the wind effects on the terahertz link with a radio unit and a dish antenna installed at the top of a pole. This configuration can be considered a possible scenario of THz links, which are expected to be small in size.

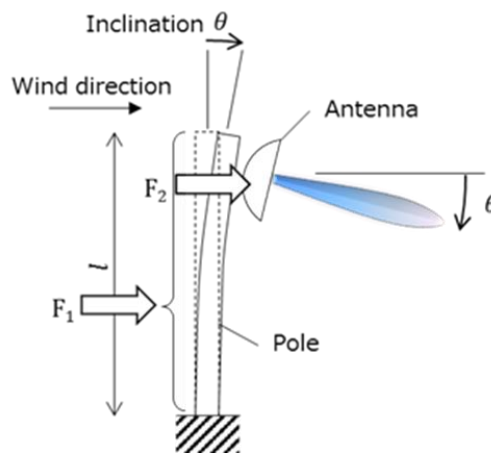


Figure 6.2.2. Model configuration

We assume the static load given to the pole and the antenna due to wind and consider it as follows. The calculation model is described in Figure 6.2.2.

6.2.1. Static component of the inclination due to wind

The inclined angle of the pole assuming the static load taken on the pole and the antenna due to wind is derived as follows.

The velocity pressure when the wind velocity is v is shown as follows.

$$q = \frac{1}{2} \rho v^2 \quad \cdot \cdot \cdot \text{Eq. 6.2.1}$$

q : Velocity pressure [N/m²]

ρ : Air density (=1.226 [kg/m³])

v : Wind speed [m/s]

The static load F_1 applied to the pole and the static load F_2 applied to the antenna are described as follows.

$$F_1 = qC_1A_1, \quad F_2 = qC_2A_2 \quad \cdot \cdot \cdot \text{Eq. 6.2.2}$$

F_1 : Wind load applied to the pole [N]

F_2 : Wind load applied to the antenna [N]

C_1 : Drag coefficient of the pole

C_2 : Drag coefficient of the antenna

A_1 : Wind receiving area of the pole [m²]

A_2 : Wind receiving area of the antenna [m²]

Inclination angle θ_s is described as follows.

$$\theta_s = \frac{F_1 l^2}{6EI} + \frac{F_2 l^2}{2EI} = (F_1 + 3F_2) \frac{l^2}{6EI} [rad] = (C_1 A_1 + 3C_2 A_2) \frac{\rho l^2}{12EI} v^2 \frac{180}{\pi} [deg] \quad \cdot \cdot \cdot \text{Eq. 6.2.3}$$

E : Young's modulus [Pa]

I : Second moment of area [m⁴]

l : Length of the pole [m]

From the above, the inclination angle θ_s is proportional to the square of the wind speed. The parameters in the measurement system are shown in Table 6.2.1. For simplification, Eq. 6.2.3 is expressed as Eq.6.2.4. The static wind load coefficient C_s in the measurement system is 4.2×10^{-4} deg/(m/s)².

Table 6.2.1. Parameters of the measurement system

Item	Value
C_1 : Drag coefficient of the pole	0.8
A_1 : Wind receiving area of the pole	0.445 [m ²]
C_2 : Drag coefficient of the antenna	1.1
A_2 : Wind receiving area of the antenna	0.07 [m ²]
E : Young's modulus	2.05×10^{11} [Pa]
I : Second moment of area	1.01×10^{-6} [m ⁴]
l : Length of the pole	5 [m]

$$\theta_s = (C_1 A_1 + 3C_2 A_2) \frac{\rho l^2}{12EI} v^2 \frac{180}{\pi} \equiv C_s \cdot v^2 \quad [deg] \quad \cdot \cdot \cdot \text{Eq. 6.2.4}$$

6.2.2. Dynamic component of the inclination due to wind

In the next section, the vibration of the pole is analysed from the measurement results in E-band. , in Japan over six months. The model of the measurement system is Figure 6.2.2. The pole was vibrating by wind at the natural frequency of 2.3 Hz and the inclination of the pole was derived from the dynamic amplitude which was filtered from the measurement results. The maximum value of the wind speed and the amplitude are adopted every ten seconds. The dynamic inclination angle θ_d of the pole is proportional to the square of the wind speed as static wind load. The coefficient C_d that shows the relationship between the wind speed and the dynamic inclination is expressed as Eq. 6.2.5. The C_d from the measured data is 4.6×10^{-4} deg/(m/s)².

$$\theta_d \equiv C_d \cdot v^2 \quad [\text{deg}] \quad \cdot \cdot \cdot \text{Eq. 6.2.5}$$

6.2.3. FWS link performance degradation

From the above, the inclination of the pole due to static and dynamic wind is modelled. The radiation pattern $g(\theta)$, where θ is the deviation angle, is expressed as Eq. 6.2.6, where J_1 is the Bessel Function of the first kind and θ_{BW} is the half power beam width. For simplification, this formula may be changed for polynomial approximation. The degradation of RSL due to wind $R(v)$ is then expressed as Eq. 6.2.7. This formula indicates the worst value of RSL against certain wind speed. Regarding the inclination of the pole, misalignment angle of θ_0 should be considered when the antenna is installed.

$$g(\theta) = 20 \log \left\{ 2 \frac{J_1(u')}{u'} \right\} \quad [\text{dB}] \quad \cdot \cdot \cdot \text{Eq. 6.2.6}$$

$$u' = \frac{60\pi}{\theta_{BW}} \sin\theta$$

$$R(v) = g(\theta_0 + (C_s + C_d)v^2) \quad [\text{dB}] \quad \cdot \cdot \cdot \text{Eq. 6.2.7}$$

Figure 6.2.4. shows the measured example of the maximum wind speed vs. the minimum RSL deviation by every ten seconds. The effect of each term and approximate curve of measurement values are also shown on Figure 6.2.4. According to Figure 6.2.4., the degradation of RSL due to misalignment of the measurement system is about 1.2 dB which corresponds to 0.28 deg., the antenna has $\theta_{BW} = 0.9$ deg. One of the factors of this differences between the two cures is that the effect of the opposite site is not considered. The coefficient C_d is similar to the coefficient C_s . Both coefficients depend on the structure of the pole, therefore strong correlation is expected and C_d can be approximated to C_s .

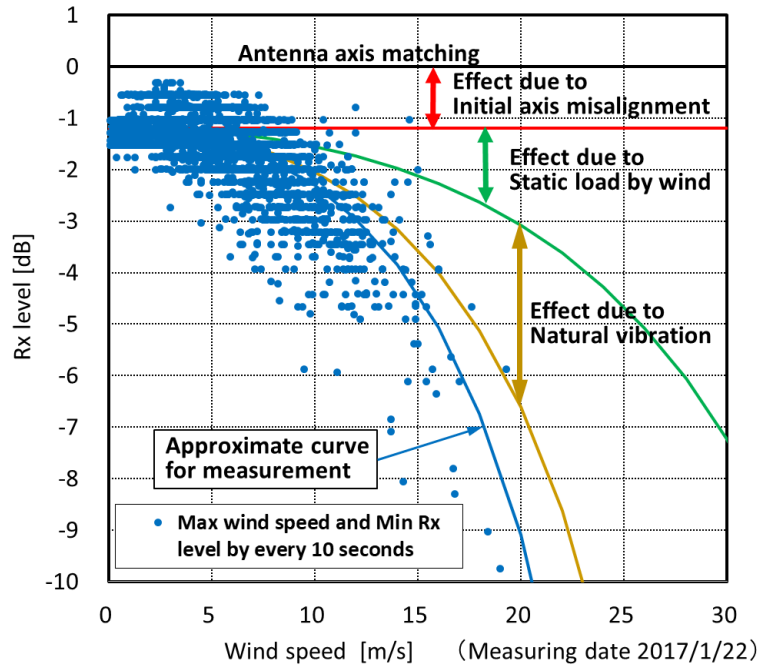


Figure 6.2.4. Measured example of Maximum wind speed vs. Minimum RSL deviation at 85.5 GHz

Regarding the opposite site, the minimum RSL is calculated as well. The worst RSL of the link R_{total} is estimated as the sum of the minimum RSL of both sites as Eq. 6.2.8, where R_1 and R_2 are the minimum RSL of respective site.

$$R_{total} = R_1 + R_2 \quad \cdot \cdot \cdot \text{Eq. 6.2.8}$$

Judging from the results discussed above, the measurement results of the inclination of the pole correspond to a good extend with the calculation model. Thus, higher frequency link like E-band or Terahertz performance degradation can be estimated from some parameters and coefficients of the link configuration.

Furthermore, the probability of the RSL is estimated from the wind speed as follows. The probability (cumulative distribution function, CDF) of wind speed is expressed by the Weibull distribution as shown in Eq. 6.2.9. An example result of this measurement is shown in Figure 6.2.5. The Weibull coefficient, scale factor k equals to 0.86 and shape factor c equals to 1.03. The wind speed corresponding to the probability of 99.999% was 17.8 m/s.

$$p(v) = 1 - \exp\left\{-\left(\frac{v}{c}\right)^k\right\} \quad \cdot \cdot \cdot \text{Eq. 6.2.9}$$

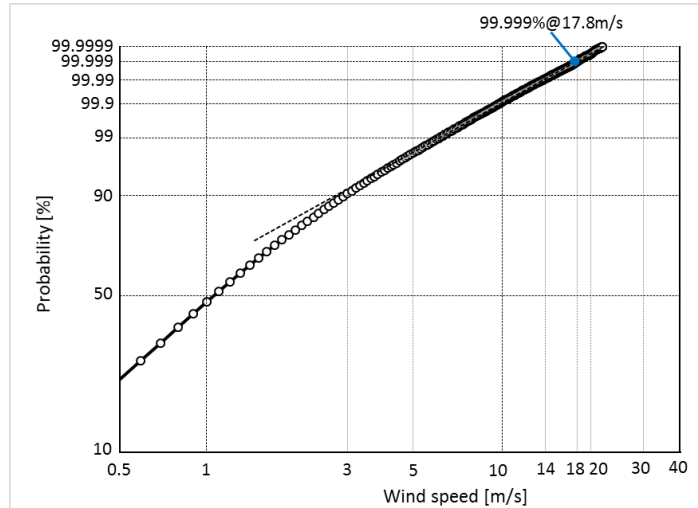


Figure 6.2.5. Wind speed distribution

The wind speed is expressed by Eq. 6.2.10 derived from Eq. 6.2.9. The relationship between cumulative probability and the degradation of the RSL is derived from Eq. 6.2.10 and Eq. 6.2.11 considering the initial misalignment of the antenna as shown in Eq. 6.2.12.

$$v(p) = c\{-\log_e(1 - p)\}^{1/k} \text{ [m/s]} \quad \cdot \cdot \cdot \text{ Eq. 6.2.10}$$

$$\theta(p) = \theta_0 + v^2(p)(C_s + C_d) \text{ [deg]} \quad \cdot \cdot \cdot \text{ Eq. 6.2.11}$$

$$R(\theta) = g\{\theta(p)\} \text{ [dB]} \quad \cdot \cdot \cdot \text{ Eq. 6.2.12}$$

Figure 6.2.6. shows the CDF of the gain degradation derived from the relationship between the wind speed and the degradation of the RSL. The initial alignment error θ_0 is considered. The model corresponds to the measured data well, though still around 1 dB difference remains.

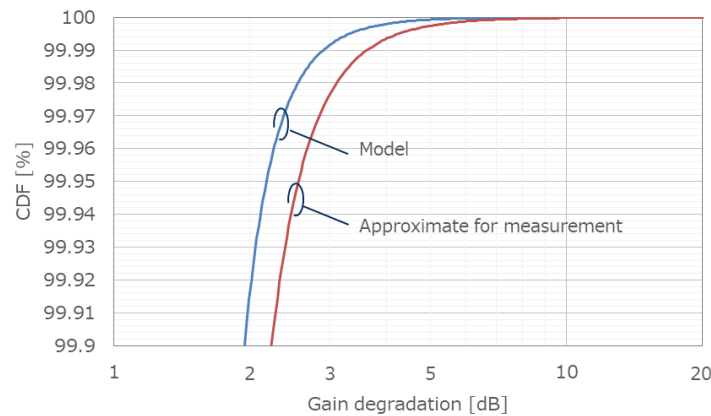


Figure 6.2.6. CDF gain degradation ($\theta_0=0.28$ deg)

The performance degradation of the link over E-band, which has narrow beam width can be estimated from some physical parameters and coefficients of the link structure.

6.2.4. Calculation examples

Six calculation examples are shown as follows. Table 6.2.2. shows the parameters of each case. The differences of the cases are pole diameter, pole length, antenna diameter and initial alignment error.

Table 6.2.2. Parameters in six cases

Item	Unit	Case 1	Case 2	Case 3	Case 4	Case 5	Case 6
Parameter of the pole							
C_1 : Drag coefficient of the pole		0.8	0.8	0.8	0.8	0.8	0.8
l : Length of the pole	m	5	5	10	5	5	10
Diameter of the pole	mm	89	89	165.2	89	89	165.2
Thickness of the pole	mm	4.2	4.2	10	4.2	4.2	10
A_1 : Wind receiving area of the pole	m ²	4.45×10^{-1}	4.45×10^{-1}	1.65	4.45×10^{-1}	4.45×10^{-1}	1.65
E : Young's modulus	GPa	205	205	205	205	205	205
I : Second moment of area	m ⁴	1.01×10^{-6}	1.01×10^{-6}	1.47×10^{-5}	1.01×10^{-6}	1.01×10^{-6}	1.47×10^{-5}
Parameter of the antenna							
C_2 : Drag coefficient of the antenna		1.1	1.1	1.1	1.1	1.1	1.1
Diameter of the antenna	m	0.32	0.32	0.32	0.65	0.65	0.65
A_2 : Wind receiving area of the antenna	m ²	8.04×10^{-2}	8.04×10^{-2}	8.04×10^{-2}	3.32×10^{-1}	3.32×10^{-1}	3.32×10^{-1}
Beam-width of the antenna	deg	0.9	0.9	0.9	0.45	0.45	0.45
C_s : Static wind load coefficient		4.40×10^{-4}	4.40×10^{-4}	3.07×10^{-4}	1.03×10^{-3}	1.03×10^{-3}	4.68×10^{-4}
C_d : Dynamic wind load coefficient		4.40×10^{-4}	4.40×10^{-4}	3.07×10^{-4}	1.03×10^{-3}	1.03×10^{-3}	4.68×10^{-4}
θ_0 : Initial alignment error	deg	0	0.2	0.2	0	0.2	0.2

The calculation results are shown as follows. The relationship between the wind speed and the inclination of the pole is calculated from Eq. 6.2.11, and the results are shown in Figure 6.2.7.

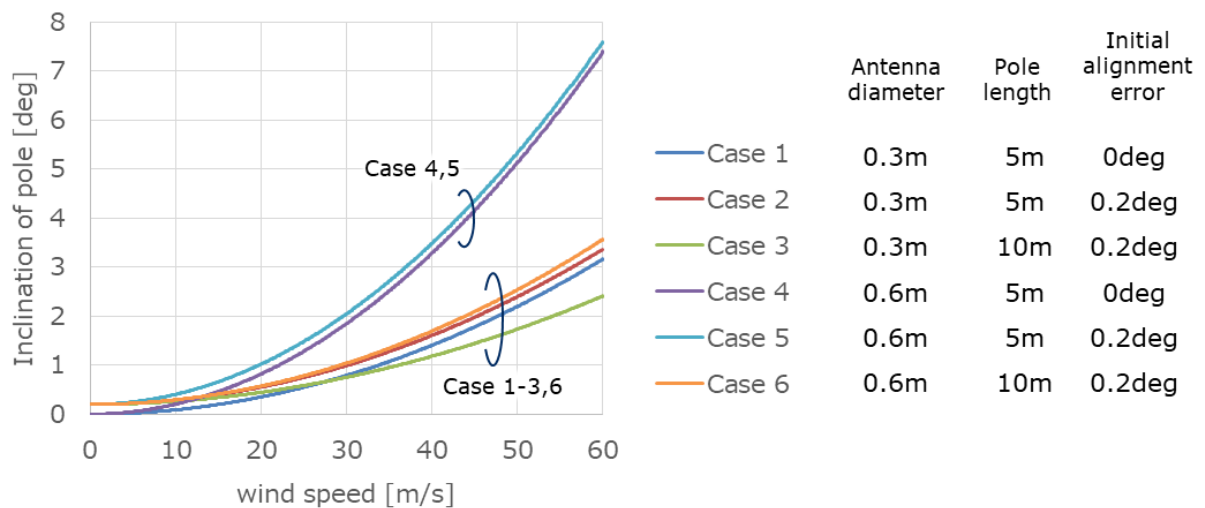


Figure 6.2.7. Inclination of pole

Figure 6.2.8. shows the corresponding gain degradation. In this figure, 0 dB means gain degradation of the 0.6-m antenna. As the wind speed becomes strong, the gain degradation of the 0.6 m-antenna becomes larger than the one of 0.3-m antenna due to the area.

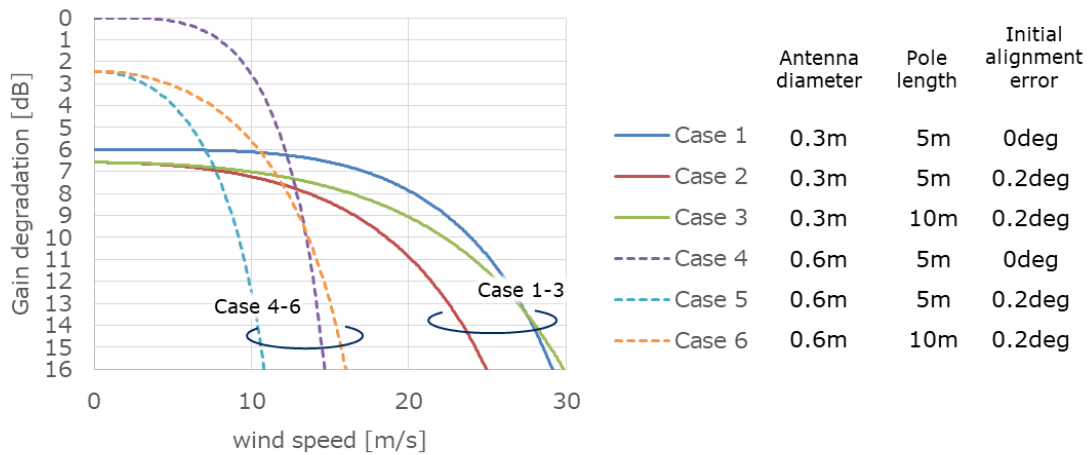


Figure 6.2.8. Gain degradation

The CDF of gain degradation is calculated from Eq. 6.2.12 and the results are shown in Figure 6.2.9. The probability of gain degradation is significant for the 0.6-m antenna, however better for the 0.3-m antenna under the strong wind condition.

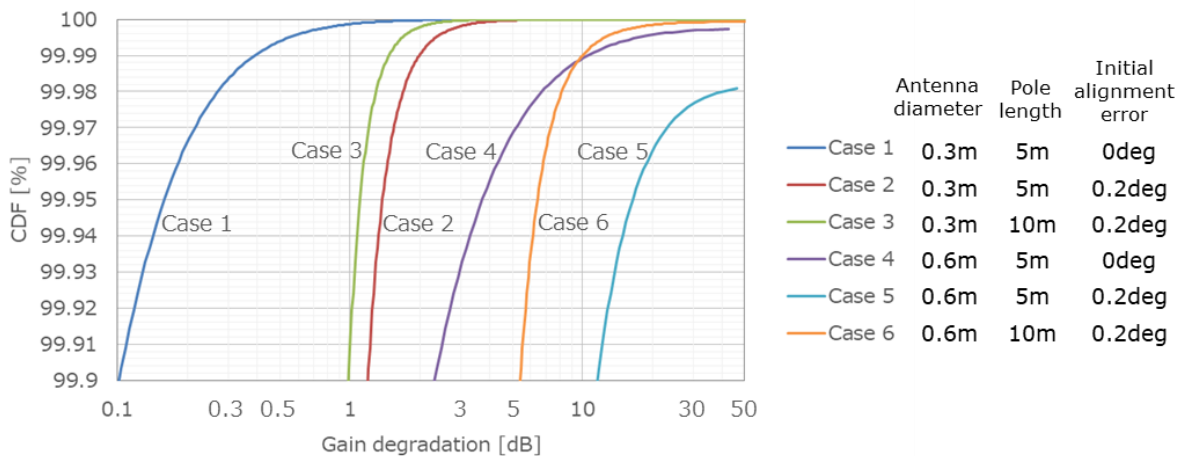


Figure 6.2.9. CDF of gain degradation

In these cases, a more robust pole is required for the 0.6 m-antenna.

This section provides the measured data and theoretical analysis method for the millimetre-wave link performance under strong wind condition. The data were measured in E-band, 84.5 GHz, however, it is possible to estimate the terahertz link performance by applying the data of the antenna radiation pattern, physical parameters of the site structure and rain fall probability at the link into the formulas.

A larger antenna, a taller pole are sensitive for wind effects. In case of such conditions, larger diameter and thickness of the pole are required. The expected performance of the design can be calculated from the equations presented in this section.

6.3. Propagation experiments

Terahertz waves have a strong straight-running property, and the diffraction at the obstacles are quite small. Therefore, THz wireless links require line-of-sight (LOS) in order to obtain sufficient received power at the receiver. These properties of THz wireless links decrease the cover area, and limits the applications. If the THz wireless link can be used in non-line-of-sight (NLOS) environment, the possibilities of application of THz wireless link can be expanded. However, there has been little investigation about the diffraction characteristics of THz waves. The clarification of the diffraction characteristics of THz waves contributes to expand the application of THz wireless links and to relax the limitation of base station deployment.

In this section, we measured the diffraction characteristics of THz waves by using the 300-GHz-band Tx/Rx described in Sec. 5.3, and compared the measured results with the radio wave propagation simulation.

Figure 6.3.1 shows the schematic diagram of the experiment for the evaluation of THz wave diffraction characteristics. The distance between Tx and Rx is 2 m and the obstacles were set at the middle of the Tx and the Rx. Orthogonal horn antennas with a gain of 25 dBi were used on both the Rx and the Tx. The Rx was moved by 50 cm with a step width of 5 cm along y axis in Fig. 6.3.1. We employed three types of obstacles in order to evaluate the effect of knife-edge diffraction. The surfaces of all obstacles are metal. The schematics of the obstacles are shown in Fig. 6.3.2.

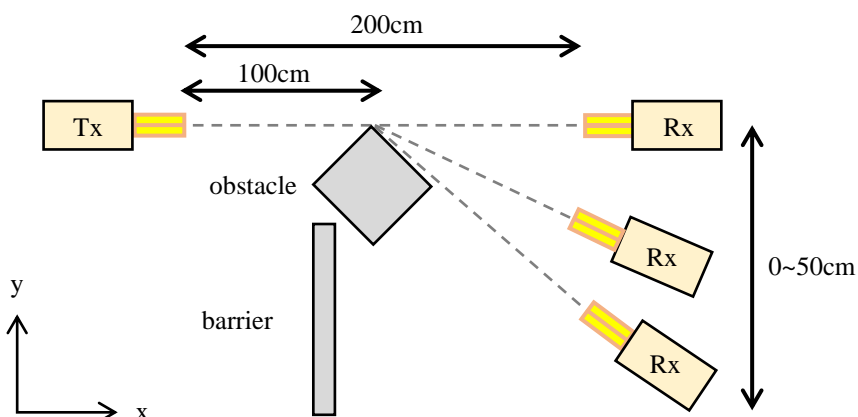


Figure 6.3.1. Schematic diagram of the experiment for the evaluation of THz wave diffraction characteristics

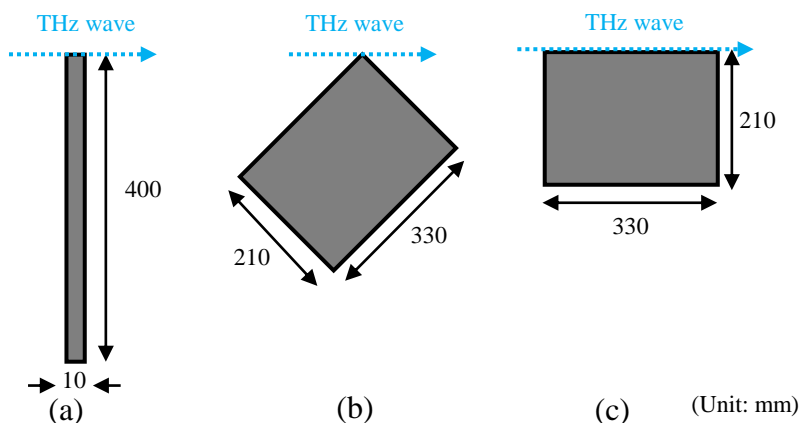


Figure 6.3.2. Schematics of obstacles

Figures 6.3.3 show the photographs of the experiment for the evaluation of THz wave diffraction characteristics. The setups with the obstacles depicted in Fig. 6.3.2 (a), (b) and (c) are shown in Fig. 6.3.3(a), (b) and (c), respectively. The obstacle (a) is a 10-mm-thick metal plate. The obstacle (b) and (c) is a box with a width of 330 mm and a depth of 210 mm. The obstacle (b) was placed at an angle of 45 degrees with respect to the direction of travel of the terahertz wave. The width of the obstacle (c) was placed parallel to the direction of travel of the terahertz wave.



Figure 6.3.3. Photographs of the experiment for the evaluation of THz wave diffraction characteristics. The obstacles (a), (b) and (c) shown in Fig. 6.3.2 are used here in Fig. 6.3.3(a), (b) and (c), respectively.

The dependence of the diffraction loss on the y-axis shift of the Rx is shown in Fig. 6.3.4. The angle of the antenna of the Rx was rotated depending on the shift distance in order to obtain the maximum received power. The diffraction loss of the obstacle (a) and (b) is almost the same, and it is about 30 dB for a y-axis shift larger than 30 cm. In case of the obstacle (c), the transmission loss is much higher than that of the obstacle (a) and (b), when increasing the y-axis shift of the RX above 25 cm. The diffraction loss for a shift distance of 50 mm is about 50 dB, which is 20 dB larger than that of the obstacles (a) and (b). These results indicate that the diffraction loss becomes large in case that the obstacle is not a knife-edge structure along the propagation path of the THz waves.

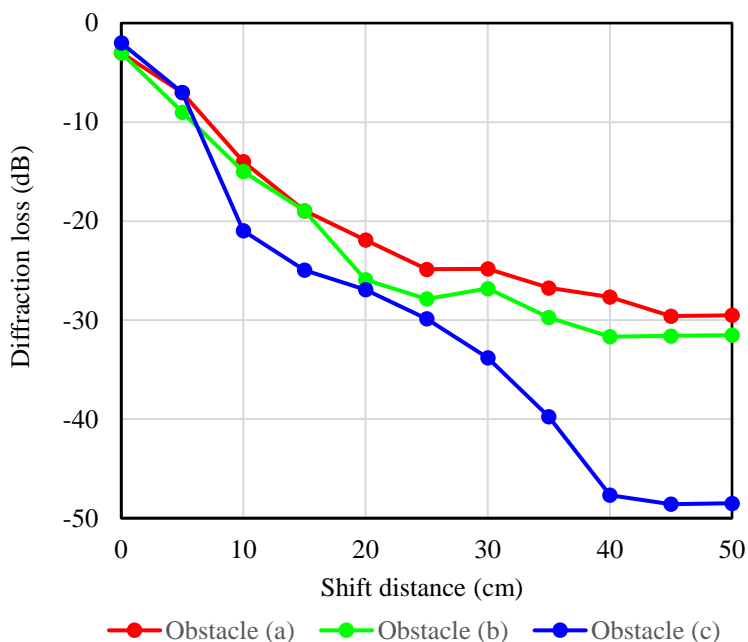


Figure 6.3.4. Dependence of diffraction loss on the shift distance

We simulated the diffraction losses by using the radio wave propagation simulator Wireless Insite. The simulation model for the evaluation of diffraction loss is shown in Fig. 6.3.5. In the simulation, the Tx and Rx employ directional antennas with a half power beam width of 10°. The simulation results of the diffraction loss as a parameter of the shift distance are shown in Fig. 6.3.6. We cannot simulate the model with the obstacles (a) and (c), because the simulator only employs the knife edge model for the simulation of the diffraction, and cannot simulate the diffraction by the obstacle whose plane is parallel to the THz wave path. The experimental results and the simulation results are in good agreement.

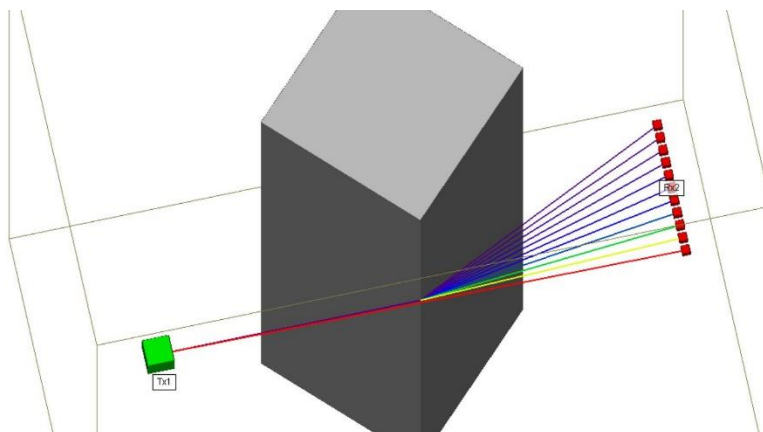


Figure 6.3.5. Simulation model that employs the obstacle (b) for the evaluation of the diffraction loss.

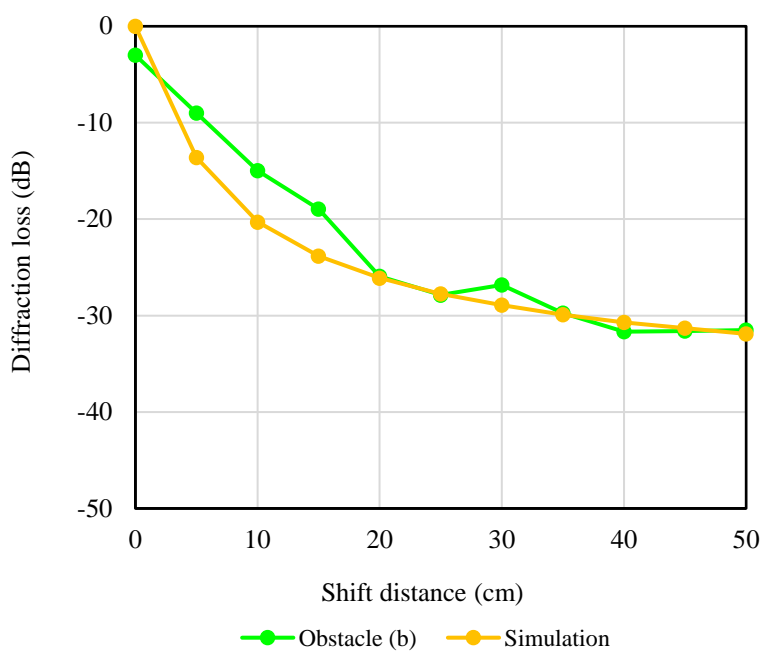


Figure 6.3.6. Simulation and experimental results of the diffraction loss for the obstacle (b).

6.4. Material Properties

In order to put the 300GHz-band wireless link into practical use, it is necessary to construct a propagation model in these bands. However, only a few experiments on radio wave propagation have been conducted so far. In particular, there is only little data available on the reflectance or transmittance of building materials in the 300 GHz band. In this section, we measured the complex permittivity of these building materials, such as concrete, glass, and granite, at 200-500 GHz by THz-TDS in order to calculate the reflectance and transmittance of building materials.

THz-TDS is one of the methods of generating and detecting terahertz wave pulses, which enables us to make time-resolved measurements of electromagnetic waves. In general ellipsometry, an electromagnetic wave is obliquely incident on a material and the reflection intensity of s and p polarization is measured. The phase difference between the reflected p-polarized and s-polarized electromagnetic waves is measured by rotating a polarizer (wire grid), and the optical constant of the material is calculated from the phase difference.

An s-polarized and p-polarized electromagnetic (EM) wave with equal amplitude and phase is injected into a sample at an incidence angle θ . The complex permittivity is calculated from the ratio of reflectance to s-polarized and p-polarized EM waves as r_s and r_p , respectively. Figure 6.4.1 shows the diagram of the measurement setup. We can calculate the complex permittivity of the sample from the ratio of r_p over r_s , using Eq.6.4.1.

$$n_2^2 = \sin^2 \theta + \frac{\sin^4 \theta}{\cos^2 \theta} \left(\frac{1 - \frac{r_p}{r_s}}{1 + \frac{r_p}{r_s}} \right)^2 = \epsilon_1 - i\epsilon_2 \quad \cdot \cdot \cdot \text{Eq. 6.4.1}$$

ϵ_1 : dielectric constant ϵ_2 : absorption coefficient

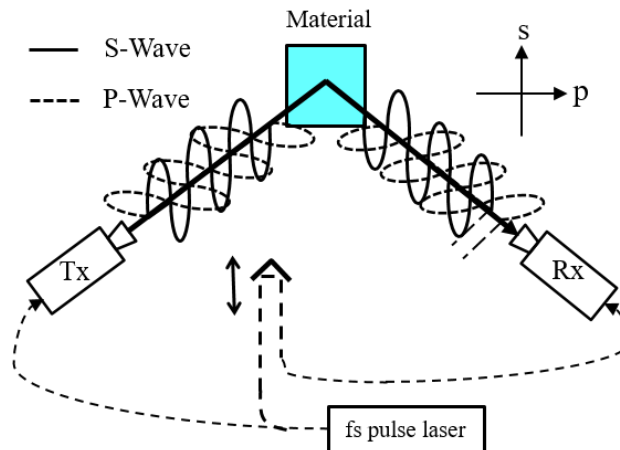


Figure 6.4.1: Experimental setup of THz-TDS.

Since Eq. 6.4.1 can only be applied to the waveform that was reflected at the surface of the sample, we need to eliminate the effect of the reflection at the backside of the sample.

Figure 6.4.2 shows the waveforms obtained by THz-TDS. The blue line shows the waveform of the reflection signal that includes the backside waveform. If we used this waveform in the ellipsometry calculation, the calculated dielectric constant fluctuates drastically depending on the frequency. In order to eliminate the effects of backside reflection, we conducted time gating to the pulse

waveform. As shown in Figure 6.4.2, we replaced the pulse waveform intensity after 536 psec with 0. The time gated waveform is shown as red line. This figure shows the real part of the complex permittivity of the plastic calculated from the time-gated waveform. The real part of the complex permittivity shows almost constant value at all frequencies.

Figure 6.4.3 shows the result of the dielectric constant of concrete calculated by applying the time gating process. In the real part, we can see the frequency dependence decreasing from 200 GHz to 300 GHz. On the other hand, in the imaginary part, the value exceeds 1 after 400 GHz. The extinction coefficient does not exceed 1. From these results, we can assume that there are other causes of influence besides back reflection.

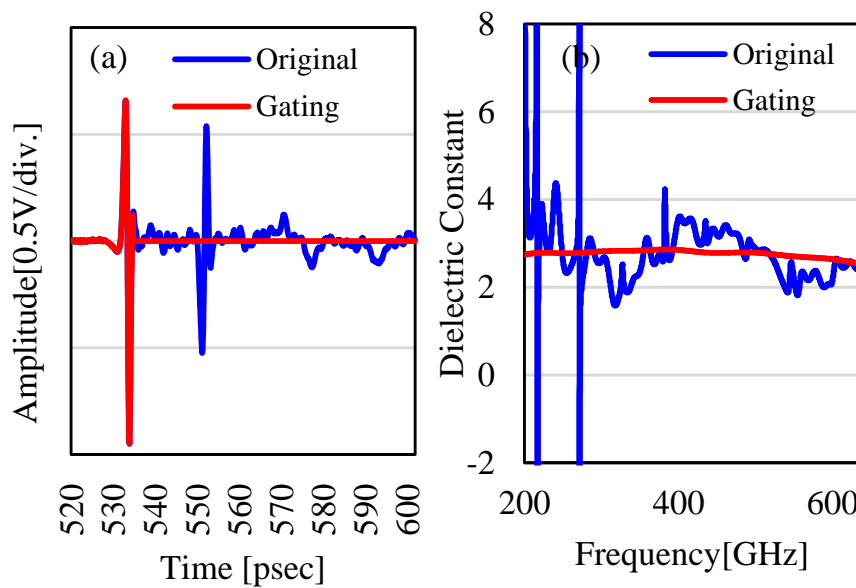


Figure 6.4.2: (a) The time domain signal that was reflected by a plastic. (b) the complex dielectric constant of the plastic that was calculated using the time-domain signals shown in Fig. 6.4.2(a).

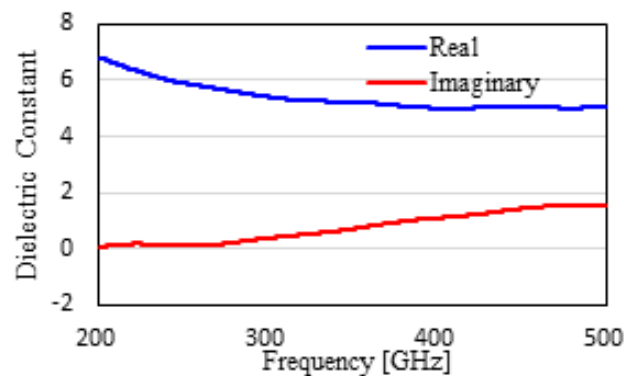


Figure 6.4.3: Complex permittivity of concrete.

Table 6.4.1 compares the complex dielectric constant at 300 GHz, where the measurement was successful, with the ITU-R value of the complex dielectric constant at 95.9 GHz. Comparing the results, the difference between our model and the ITU-R model is within 1.0 for all building materials, and the values are almost the same.

Table. 6.4.1 Complex permittivity of the building materials.

	Our Model (@300GHz)	ITU-R Model (@95.9GHz)
Concrete	5.42 – j0.38	6.20 – j0.34
Glass	6.67 – j0.008	6.76 – j0.19
Plastic	2.96 - j0.48	
Teflon	2.08 – j0.002	
Granite	5.69 – j0.02	

We also measured the complex dielectric constant by using the VNA and the transmitted signals. The experimental setups are shown in Fig. 6.4.4. THz-TDS has the advantage of ultra-wide band operation, such as from 0.1 to 1THz. In contrast, a VNA is a band-limited measurement system, which is, however, very stable and can obtain high-accuracy results.

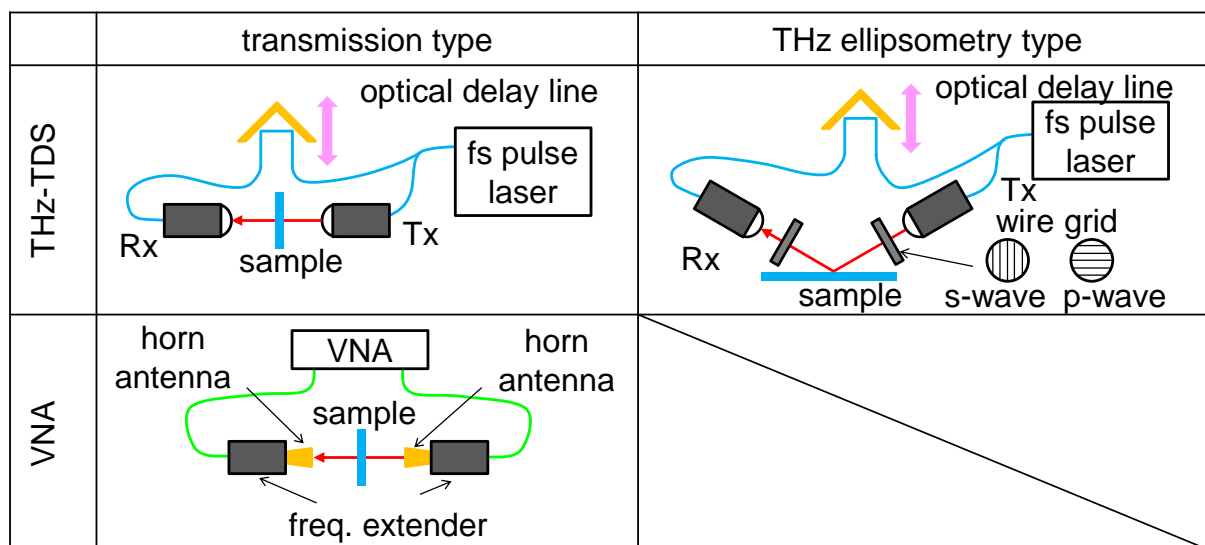


Figure 6.4.4: Experimental setup for the evaluation of complex dielectric constant.

We can calculate the complex permittivity from the transmission characteristics by using equation 6.4.2. Therefore, we measured the transmission characteristics of glasses using THz-TDS and the VNA. This technique can be applied for the materials that allow terahertz waves to pass through, and cannot be employed for the samples that do not transmit THz signal, such as concrete.

$$\left(x + \frac{1}{x}\right) \sinh(xP) + 2 \cosh(xP) - \frac{2}{s_{21}} = 0 \quad \cdot \cdot \cdot \text{Eq. 6.4.2}$$

$$x = \sqrt{\varepsilon_1 - i\varepsilon_2}, P = j\beta_0 d, \beta_0 = 2\pi f/c, d: \text{glass thickness, } c: \text{speed of light}$$

Figure 6.4.5 shows the complex permittivity of heat ray absorbing plate glass with a thickness of 3.0 mm. The complex permittivity was obtained by ellipsometry measured by THz-TDS. Heat ray absorbing plate glass is a float plate glass in which metal ions are doped. The reflected pulse signal was time-gated with a width of 10 ps in order to eliminate the reflection signal at the backside of the glass. The real part of the permittivity decreases from 6.3 to 5.0 at 200-500 GHz, and the imaginary part of the glass is found to be between 0.35 and 0.50 at 200-500 GHz.

Figure 6.4.5 also shows the complex permittivity of the same heat ray absorbing plate glass calculated from the transmission characteristics measured by THz-TDS and VNA. The glass permittivity measured by THz-TDS and VNA are in very good agreement, and both the real part and the imaginary part of the complex permittivity is almost constant at 200-500 GHz. The real part and imaginary part of the permittivity is about 6.3 and 0.3, respectively.

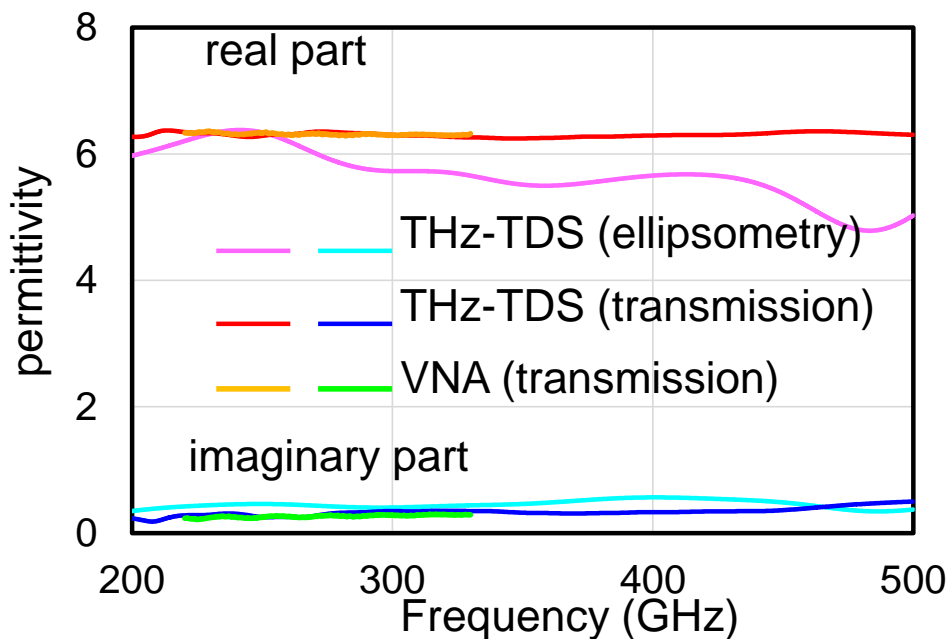


Figure 6.4.5 Complex permittivity of the heat ray absorbing plate glass

Figure 6.4.6 shows the complex permittivity of the float plate glass and frosted float plate glass that were measured by THz-TDS. The surface roughness of the frosted glass was 3-10 μm . The complex permittivity is smaller than that of the heat ray absorbing plate glass (real part: 5.8, imaginary part: 0.28 @300 GHz). The complex dielectric constant of the glass and the frosted glass is almost the same at 200-500 GHz. These results indicate that the glass surface roughness of 3-10 μm does not affect the complex permittivity measurement.

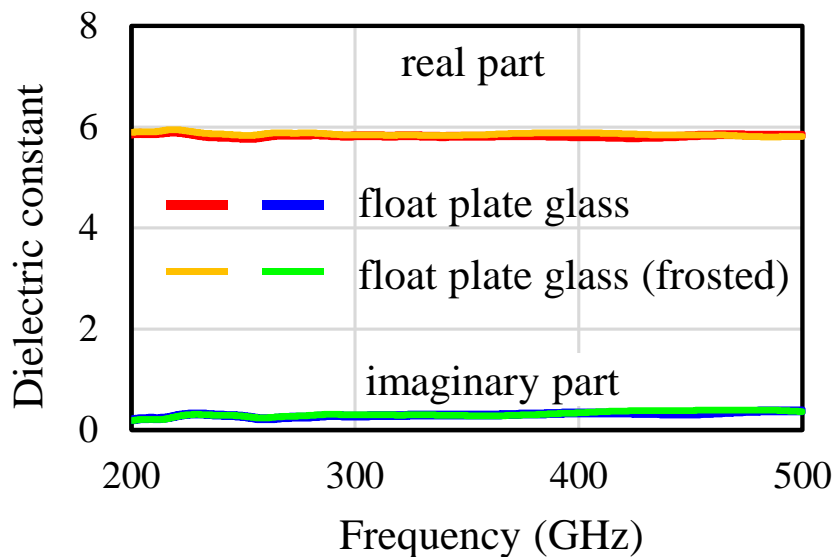


Figure 6.4.6 Complex permittivity of the float plate glass and the frosted float plate glass calculated from the transmission characteristics measured by THz-TDS.

6.5. Path loss prediction based on measured weather data

6.5.1 Comparison of ray optical results considering general local weather conditions

We conducted path loss investigation to design THz links which offer stable data transmission under various weather conditions, including heavy rain, strong storm, etc. In THz bands, attenuation by gas absorption of the air is much larger than in conventional bands including millimetre-wave bands. As shown in Figure 6.5.1, free space path loss (FSPL) is also much larger in the THz region than in lower frequency bands. In addition to attenuation of radio-waves due to rain attenuation which has been studied for many years, wind effect should be considered to investigate path loss under severe weather condition, such as storm. As discussed in section 6.2, excess loss due to mechanical vibration of antennas should be taken into account to design reliable THz transmission links dedicated to outdoor uses.

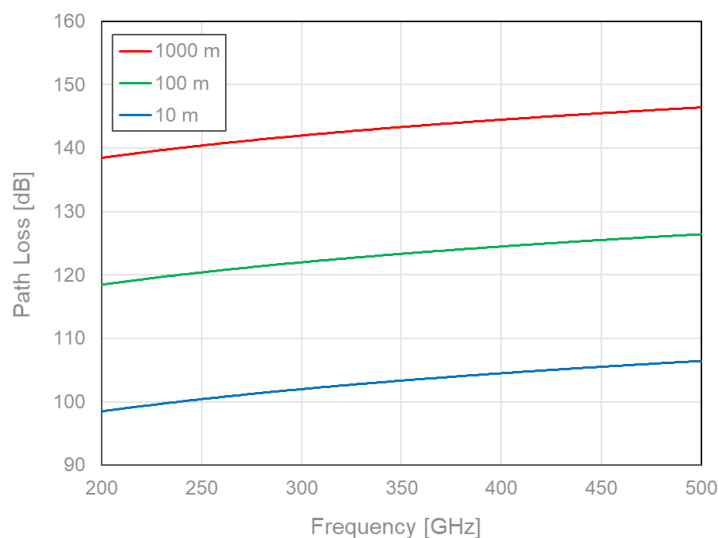


Figure 6.5.1 Free space path loss for various transmission lengths: 1000m, 100m and 10m.

This section describes the path loss analysis results which include gas absorption, rain attenuation and mechanical vibration due to wind, to offer a guideline to design robust THz transmission systems. An ITU recommendation [6.5.1] offers numerical models for gas absorption in the air, while rain attenuation can be calculated by using [6.5.2]. Figure 6.5.2 shows path loss due to gas absorption and rain attenuation calculated by the two ITU-R recommendations, for various weather conditions. The standard atmosphere is defined in [6.5.3]. We also defined the following three cases: Summer, Storm and Winter, as shown in Table 6.5.1. In the case of Storm, we should consider rain attenuation which can be calculated by using [6.5.2]. The dashed orange curve is attenuation without rain attenuation, while the solid orange curve shows the total attenuation caused by gas absorption and rain attenuation. Losses due to rain attenuation for light rain (5mm/h) and heavy rain (50mm/h) are also shown as a blue and purple dashed curve in Figure 6.5.2.

To include wind effect, we should consider misalignment of the antenna direction induced by mechanical vibration. As described in section 6.2, the maximum misalignment angle which should be considered would be 0.4 degree to ensure 99.999% availability. By using antenna patterns, the expected misalignment can be converted into loss due to strong wind. *Recommendation ITU-R F.699-8, Reference radiation patterns for fixed wireless system antennas for use in coordination studies and interference assessment in the frequency range from 100 MHz to 86 GHz* offers reference antenna patterns to design radio links or to investigate potential interferences. Figure 6.5.3 shows antenna patterns for 50-dBi, 30-dBi and 15-dBi antennas, calculated by using the reference model defined in the ITU-R recommendation. However, this recommendation only covers

frequency range up to 86 GHz. Studies of antenna models for the THz bands are still underway in ITU-R. We performed a link budget analysis for THz fixed wireless links using 50-dBi antennas both at the transmitter and receiver sides. Figure 6.5.4 shows the expected excess loss due to wind, where 0.4-degree misalignment should be taken into account to ensure 99.999% availability. The loss would be 9.0dB at each antenna. Hence, in the worst case, the total loss which occurs at both antennas at the transmitter and the receiver side should be 18.0dB.

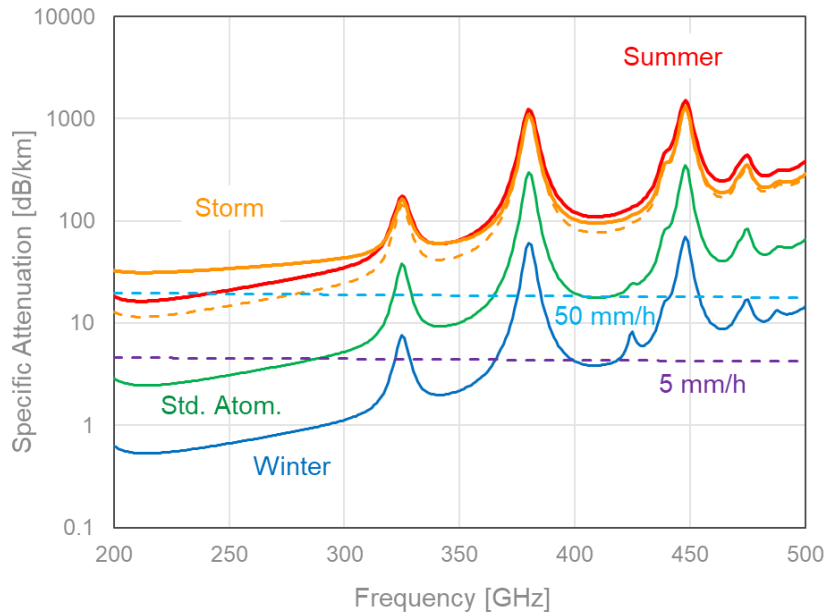


Figure 6.5.2 Path loss due to gas absorption and rain attenuation.

Table 6.5.1 Weather condition models: Summer, Storm, Standard Atmosphere and Winter.

Weather	Temp. [°C]	Hum. [%]	Press. [hPa]	Rain [mm/h]
Summer	40	80	1050	0
Storm	30	100	950	50
Std. Atom.	15	58.2	1013.15	0
Winter	0	30	1050	0

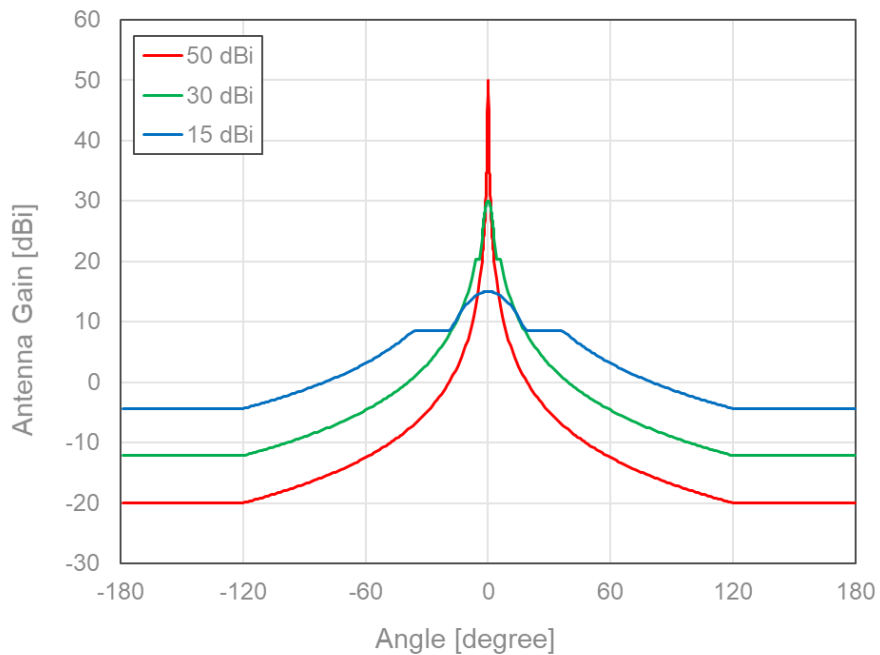


Figure 6.5.3 Reference antenna patterns for 50-dBi, 30-dBi and 15-dBi antennas.

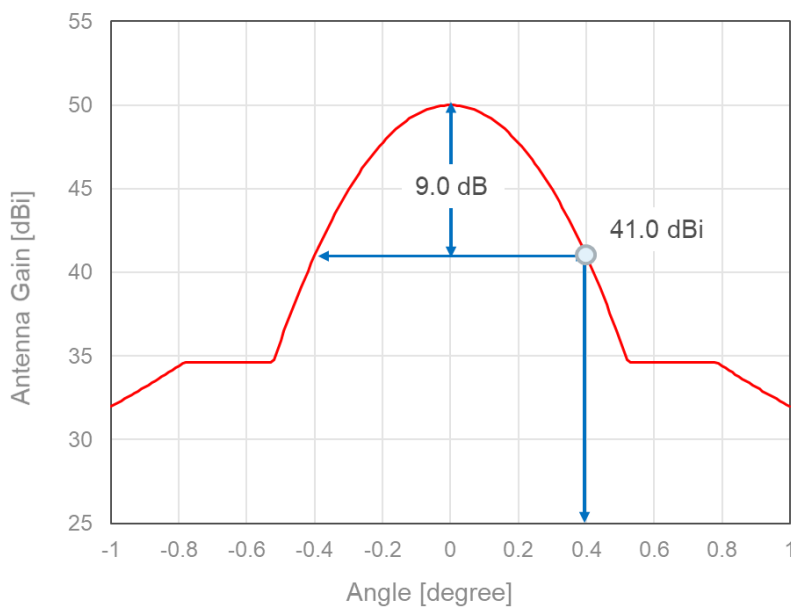


Figure 6.5.4 Expected loss due to 0.4-degree misalignment. The antenna gain is 50 dBi.

Here, we discuss the SNR degradation due to gas absorption, rain attenuation and wind effect. Figure 6.5.5 shows the SNRs of fixed wireless links whose carrier frequency is 300GHz, for Standard air (std) and Storm (storm) conditions. Rain rates are assumed to be 0mm/h, 5mm/h and 50mm/h. Signal bandwidths are set to an integer multiple of 2.16GHz (2.16GHz, 12.96GHz and 51.84GHz). The transmitted THz signal power is assumed to be 20dBm.

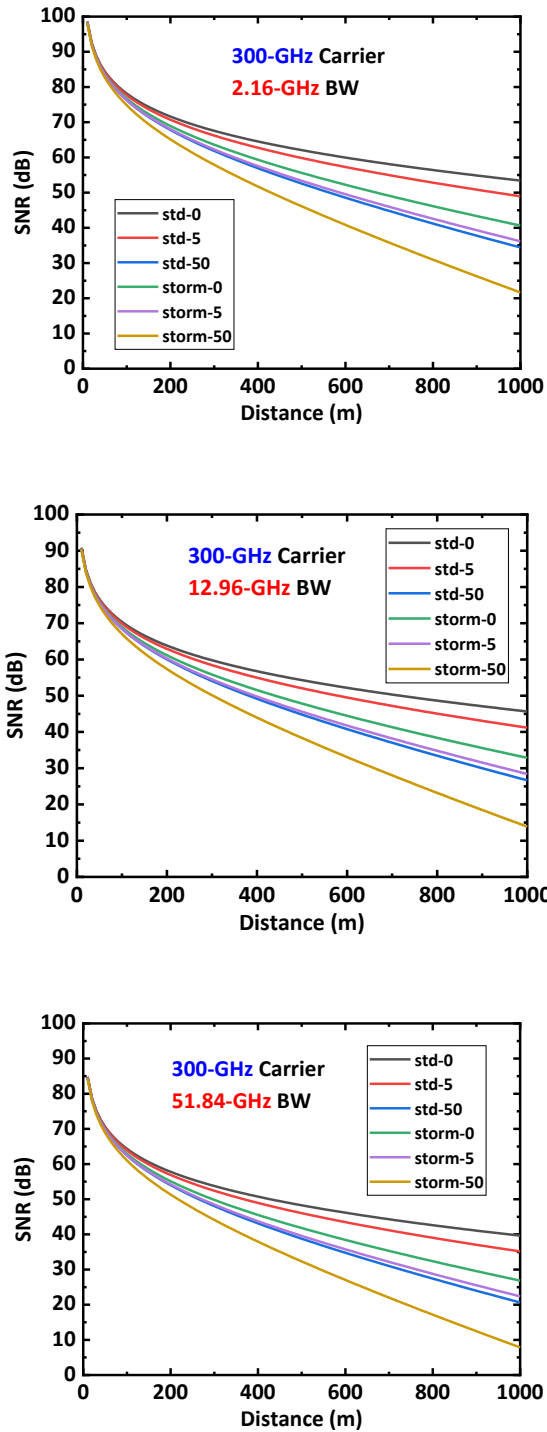


Figure 6.5.5 SNRs of fixed wireless links using a 300 GHz carrier. BWs are 2.16GHz (upper), 12.96GHz (middle) and 51.84GHz (lower).

Figure 6.5.6 and Figure 6.5.7 show SNRs for 356GHz and 410GHz carriers, which correspond to relative minimum propagation losses close to 350GHz and 400GHz as shown in Figure 6.5.2. The SNRs do not include the excess loss caused by mechanical vibration due to strong wind, while Figures 6.5.8-10 show SNRs with the vibration effect (18-dB additional loss).

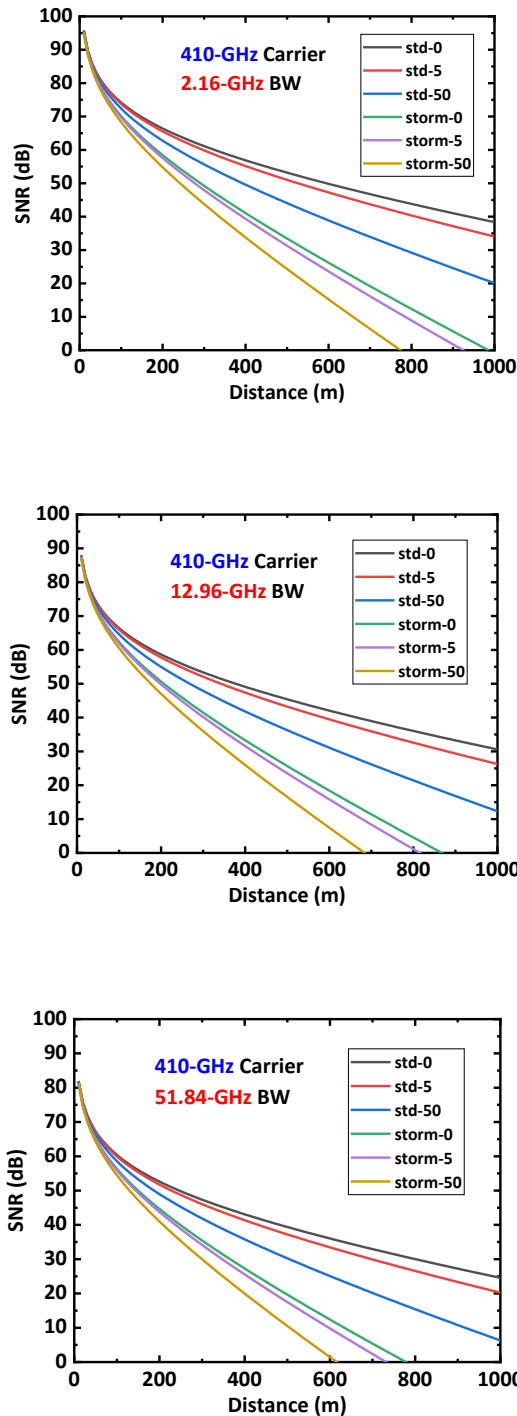


Figure 6.5.6 SNRs of fixed wireless links using 356 GHz carrier. BWs are 2.16GHz (upper), 12.96GHz (middle) and 51.84GHz (lower).

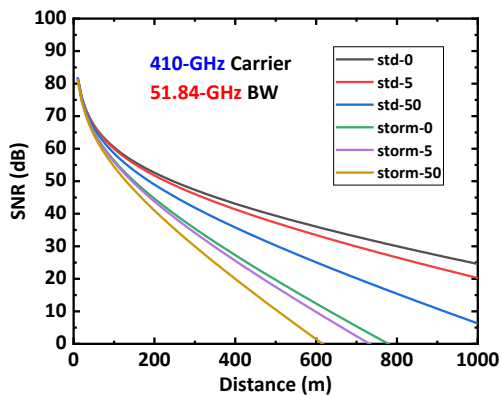
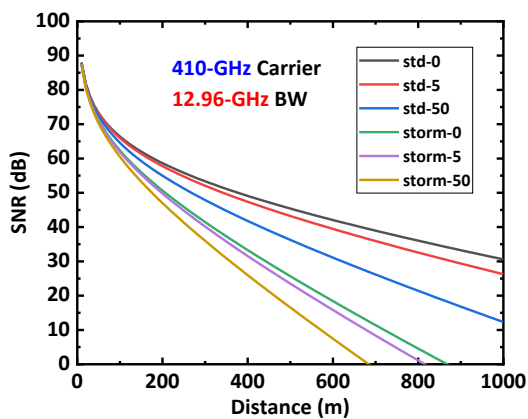
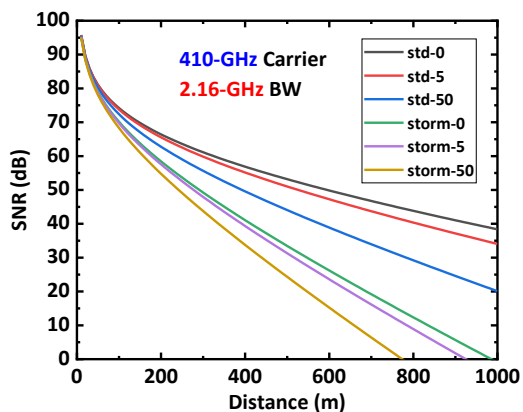


Figure 6.5.7 SNRs of fixed wireless links using 410 GHz carrier. BWs are 2.16GHz (upper), 12.96GHz (middle) and 51.84GHz (lower).

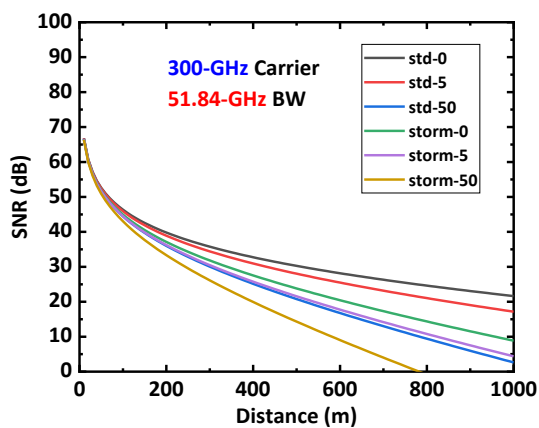
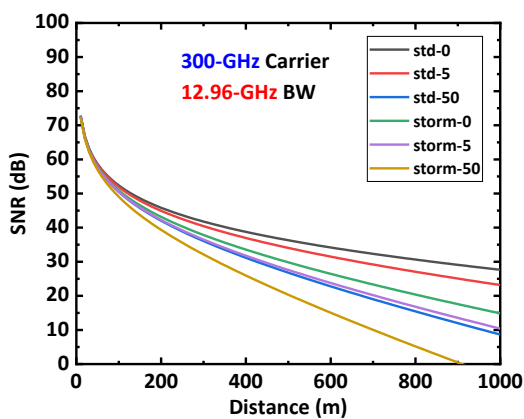
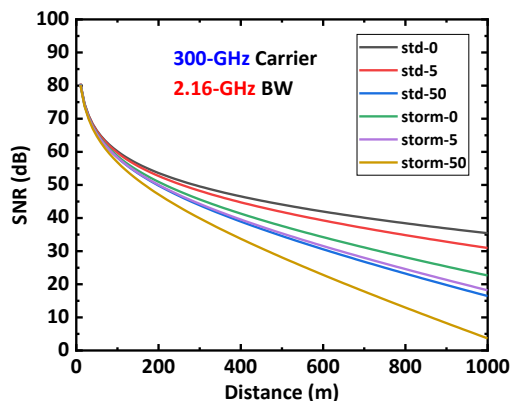


Figure 6.5.8 SNRs of fixed wireless links using 300 GHz carrier. BWs are 2.16GHz (upper), 12.96GHz (middle) and 51.84GHz (lower). Wind effect is included.

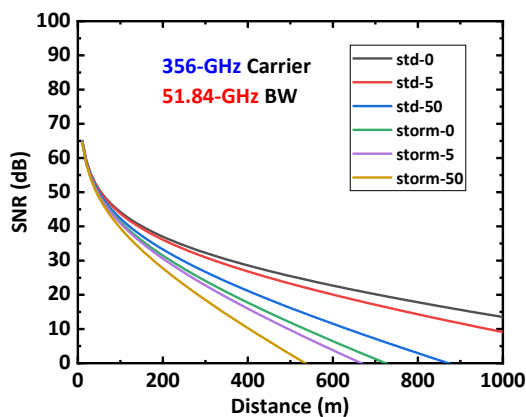
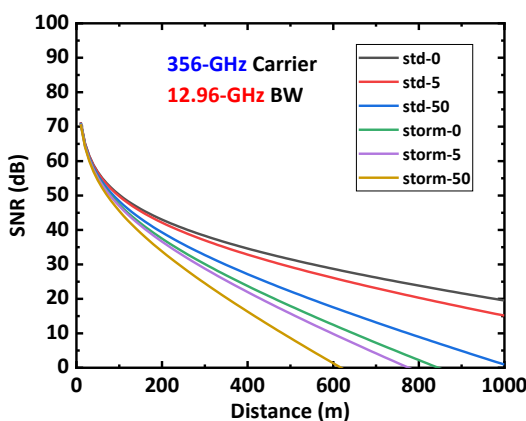
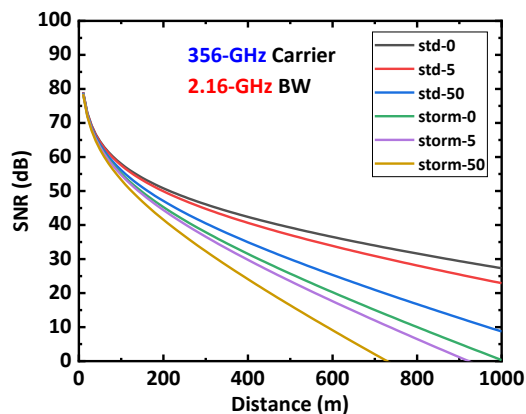


Figure 6.5.9 SNRs of fixed wireless links using 356 GHz carrier. BWs are 2.16GHz (upper), 12.96GHz (middle) and 51.84GHz (lower). Wind effect is included.

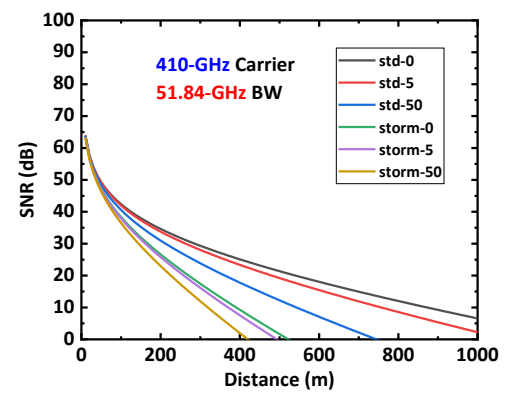
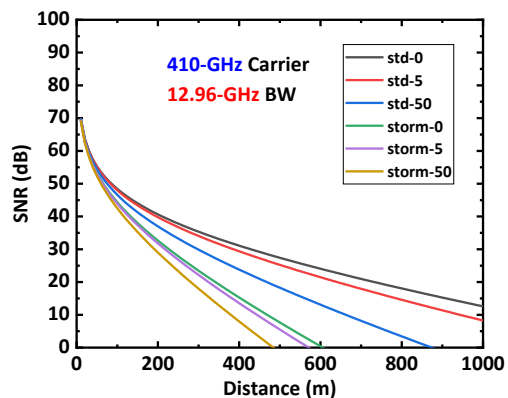
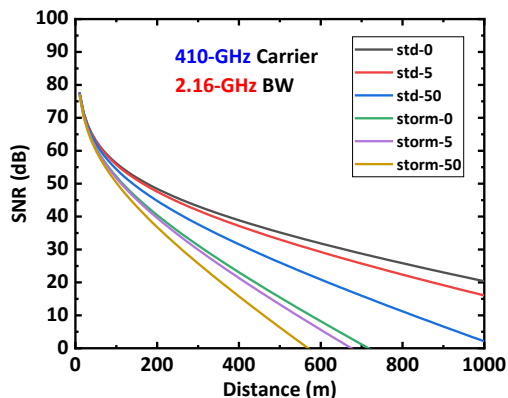


Figure 6.5.10 SNRs of fixed wireless links using 410 GHz carrier. BWs are 2.16GHz (upper), 12.96GHz (middle) and 51.84GHz (lower). Wind effect is included.

Here, we consider the expected transmission distance for fixed wireless links using QPSK whose required SNR is approximately equal to 10dB. We assume the receiver SNR is 15dB as defined in [6.5.4]. Thus, the total required SNR would be 25dB. Figure 6.5.11 shows SNRs for Standard Air no rain, Storm with and without vibration. The storm condition includes attenuation due to 50mm/h rainfall, in order to estimate the expected transmission distance under severe weather conditions.

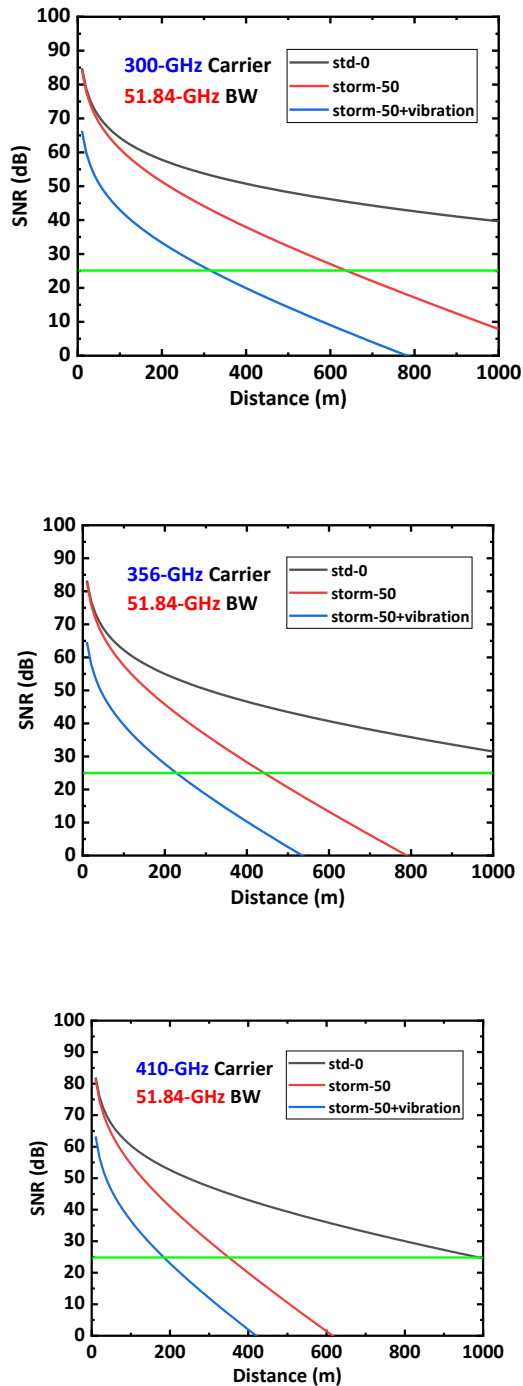


Figure 6.5.11 SNRs of fixed wireless links whose carrier frequencies are 300GHz (upper), 356GHz (middle) and 410GHz (lower), for Standard Air no rain, Storm with and without vibration. Storm condition includes attenuation due to 50mm/h rainfall.

Table 6.5.2 Expected transmission distance under various weather conditions.

	300 GHz	356 GHz	410 GHz
Standard air w/o rainfall	over 1 km	over 1 km	1 km
Storm w/ 50 mm/h rainfall	636.3 m	440.5 m	349.5 m
Storm w/ 50 mm/h rainfall + vibration	314.4 m	228.9 m	183.5 m

Table 6.5.2 summarizes the expected transmission distance which can be read from Figure 6.5.11. The SNR would be degraded due to gas absorption, rain attenuation and wind induced vibration. However, 300GHz THz links can offer over 300m transmission distance under very severe weather condition, where the transmission data rate would be close to 100Gb/s using QPSK with 51.84GHz BW. Furthermore, 400-GHz frequency bands can offer a few hundred-meter-long robust wireless transmission links.

6.5.2. Comparison of ray optical results considering general local weather condition

We simulated path loss predictions using SiMoNe. The simulations are completed in the region of Shinjuku. For the simulations, a potential pair of cell sites is chosen within a pre-designed scenario defined in [6.5.5] and its coordinates are given in Table 6.5.3.

Table 6.5.3: Positions of link pair in the unit of UTM coordinate system

	X coordinate	Y coordinate	Z coordinate
MCS1	381542.4299	3950543.883	87.5
SCS1	381414.477	3950546.992	4

MCS1 refers to the typical cell site that is mounted above rooftops of the buildings. It serves to supply mobile access environments. The backhaul link of MCS1 is thus provided via fibre connection. SCS1 refers to the lamp site which is oriented for the small mobile network coverage which will be potentially utilized in forthcoming mobile-network generations. This means that SCS1 is a typical cell site which will be potentially set up in the future and thus the provision approach of the backhaul link is not decided yet. In this case, MCS1 can thus provide the backhaul to SCS1 with a one hop connection through a wireless channel.

Figure 6.5.12 shows the entire scenario in the Shinjuku area which is defined in [6.5.5]. Both of MCS1 (coloured in red) and SCS1 (coloured in blue) are located inside of the red dotted box. The ray tracing between two cell sites is conducted considering the surfaces of every building and the ground which can be found within the entire scenario. For that, only reflection is considered as interactions of rays against materials and it is limited by 1st order reflection paths.

We conducted two simulations for predicting the propagation loss. One considers only free space path loss while the other includes weather attributes whose model is proposed in chapter 6.1. We used weather data from Raspisaniye Pogodi Ltd. [6.5.6] who provides worldwide weather data complimentary. We used weather data observed at a weather station in Tokyo positioned at N 35° 41.430000 E 139° 45.660000 (WGS84) at a height of 36 m. The weather data is collected from 01 January 2010 to 31 December 2020 over ten years with three hours resolution. To reflect and cover the general weather condition in this area, we chose a data slot which indicates the highest values of wind speed and mapped the highest precipitation value over this chosen slot. Doing this, a quasi-

authentic weather data can be achieved which can however cover general weather conditions which provoke high additional attenuation. The values of the applied weather data are given in table 6.5.4.

Table 6.5.4: Values of the applied weather data

Parameter	Value
Air pressure [hPa]	982.6
Water vapour density [g/m ³]	19.7
Rain rate [mm/h]	65
Temperature [°C]	24.3
Wind speed [m/s]	15

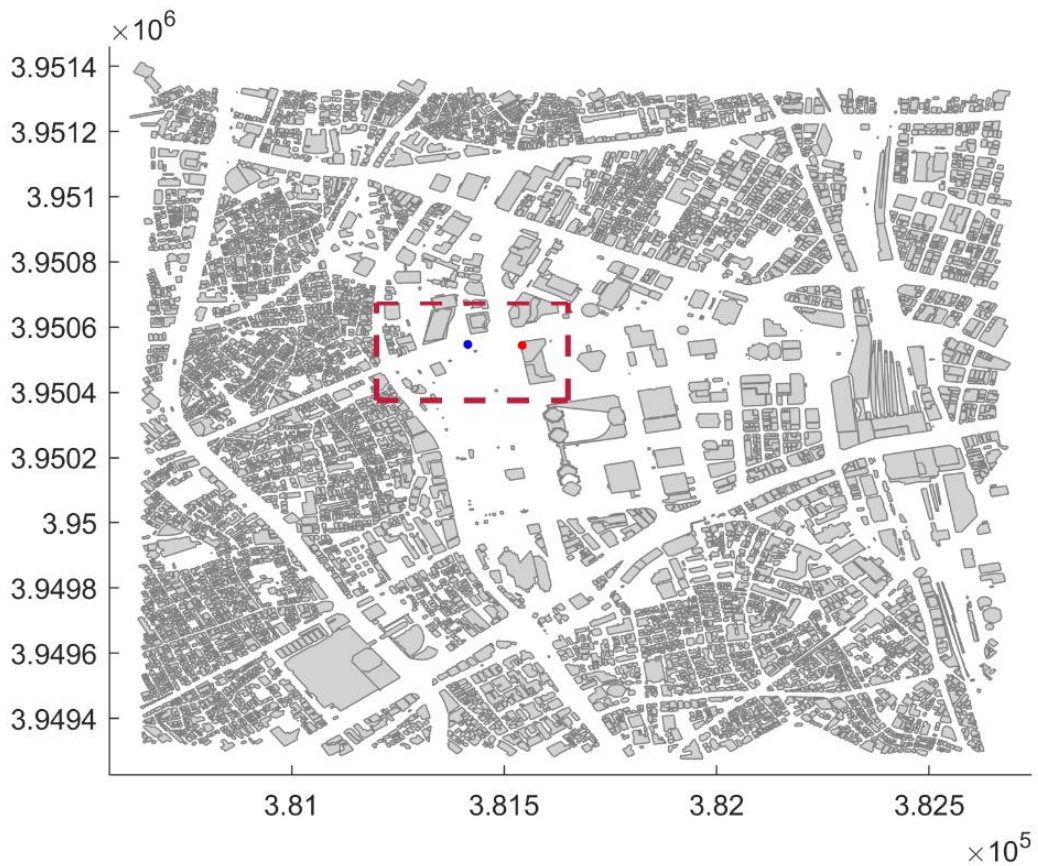


Figure 6.5.12: 2D map of the simulation scenario in Shinjuku area

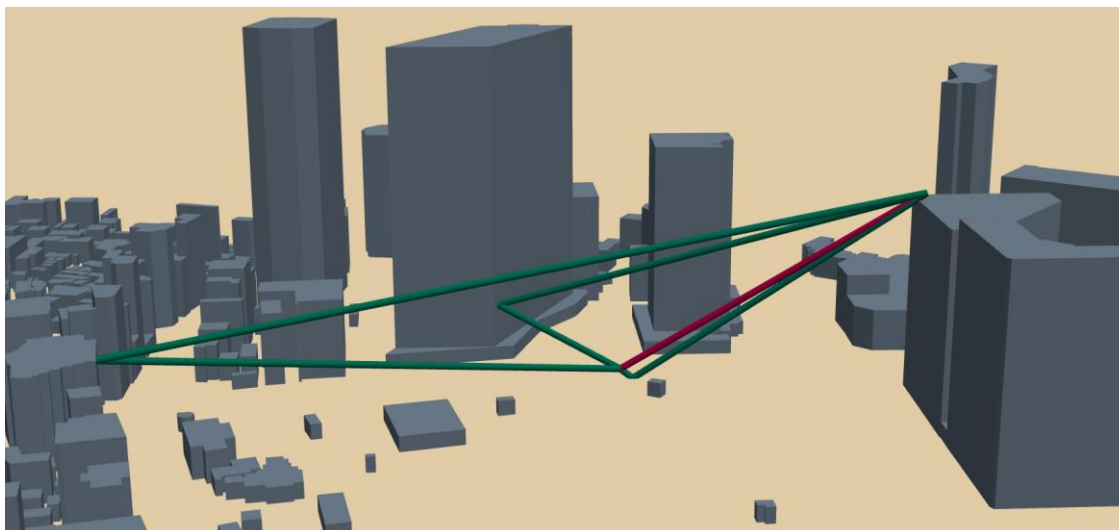


Figure 6.5.13: Point-to-point simulation result based on ray optical method

Figure 6.5.13 shows the point-to-point simulation result between two given cell sites (MCS1, SCS1) in a 3D view that is completed using ray optical method. The visualization bounding box of figure 6.5.13 corresponds to the red dotted box indicated in figure 6.5.12. Under given simulation environment, a total of four paths is revealed including one LoS path and three NLoS paths which are reflected from the ground and external surfaces of buildings.

Table 6.5.5 shows the ray tracing results in case that 50 dBi gain antennas both on the Tx and Rx are applied. The main lobes of antennas are aligned in LoS direction and the transmission power is assumed as 0 dBm. Here, the radiation pattern of the antenna is used which is recommended in [6.5.7], [6.5.8].

Table 6.5.5 Comparison of received power with and without using weather condition

		Ray 1 (LoS)	Ray 2 (NLOS)	Ray 3 (NLOS)	Ray 4 (NLOS)
TX		MCS1			
RX		SCS1			
Path length [m]		152.82	157.33	264.3	559.01
AoD [°]	Azimuth	271.4	271.4	277.6	250.9
	Elevation	33.1	35.6	18.4	8.6
AoA [°]	Azimuth	91.4	91.4	290.3	239.1
	Elevation	-33.1	35.6	-18.4	-8.6
Received power [dB]	No Weather	-25.67	-117.04	-156.22	-169.47
	With weather	-31.41	-122.88	-166.03	-190.27

The additional attenuation triggered by weather conditions (gaseous attenuation, rain attenuation) corresponds to 14.9 dB/km and 22.4 dB/km, respectively. The inclination angle of the antenna pole corresponds to 0.0048 degree and thus leads the diminutive power degradation. This is because

that 15 m/s of wind speed was not enough to sway the antenna pole strongly whose height is assumed as 1 m.

Here, ray tracing results show that received power levels of multi-paths (Ray 2-4) are low enough compared with main signal (Ray 1) as if these can be treated as noise which would not highly interfere the main signal. It is true that weather conditions induce additional power loss of the signal. Nonetheless this can be possibly minimized when the THz link is regulated as short as possible. If so, THz links would be tolerable against the general changes of weather conditions when the appropriate safety margin is considered to calculate the link budget.

REFFERECES.

- [6.5.1] Recommendation ITU-R P.676-12, "Attenuation by atmospheric gases and related effects", August, 2019.
- [6.5.2] Recommendation ITU-R P.838-3, "Specific attenuation model for rain for use in prediction methods"
- [6.5.3] Recommendation ITU-R P.835-5, "Reference Standard Atmospheres."
- [6.5.4] Report ITU-R F.2416, "Technical and operational characteristics and applications of the point-to-point fixed service applications operating in the frequency band 275-450 GHz."
- [6.5.5] ThoR D2.4, "Definition of Scenarios for Demonstration and Simulation", July, 2018.
- [6.5.6] [https://rp5.ru/Weather_archive_in_Tokyo_\(weather_station\)](https://rp5.ru/Weather_archive_in_Tokyo_(weather_station))
- [6.5.7] Recommendation ITU-R F.699-8, "Reference radiation patterns for fixed wireless system antennas for use in coordination studies and interference assessment in the frequency range from 100 MHz to 86 GHz," January. 2018.
- [6.5.8] ITU-R F.1245-3, "Mathematical model of average and related radiation patterns for point-to-point fixed wireless system antennas for use in interference assessment in the frequency range from 1 GHz to 86 GHz," January, 2019.

6.6. Simulation results

We conducted indoor radio wave propagation simulations using the measured complex permittivity of concrete and glass at 300 GHz shown in Section 6.4 and compared the simulation results that employ ITU-R material property models. Figure 6.6.1 shows the simulation model. The size of the room is 20 m x 60 m x 3 m. The height of Tx and Rx is 2 m, and omni-directional antennas with an E-plane half power beam width of 10 degree are used for the Tx and Rx. The carrier frequency is 300 GHz and the Tx output power is 10 dBm. The walls of the room are set to be concrete, and we set a glass (40 m x 1 m) that employs our material property model on the wall.

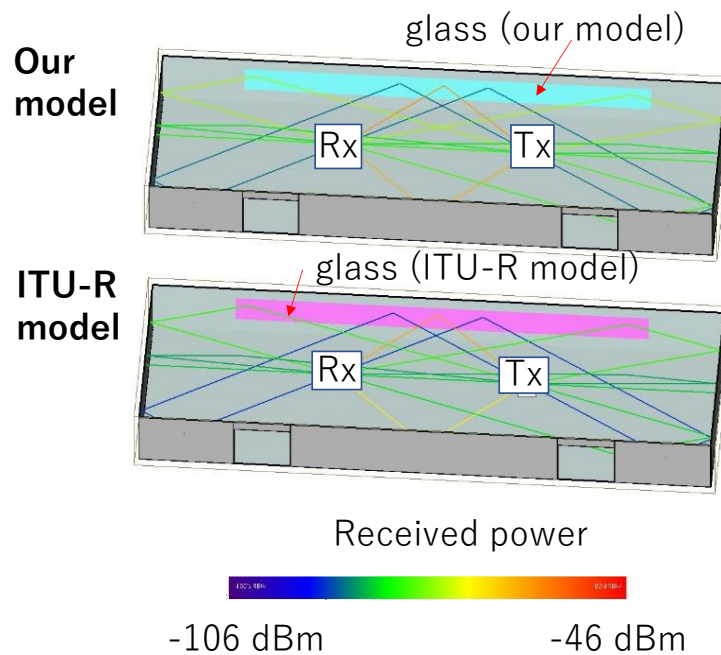


Figure 6.6.1: Simulation results of propagation paths using (a) our model and (b) ITU-R model.

Figure 6.6.2(a) and Fig. 6.6.2(b) show the simulation results of received power map that employs our material property model and ITU-R material property model, respectively. There is little difference of received power map around the transmitter. However, compared with the ITU-R model, the received power of our model is higher in many areas at the left side of the room. These results indicate that the reflection at high incident angle in our model is larger than that of ITU-R model.

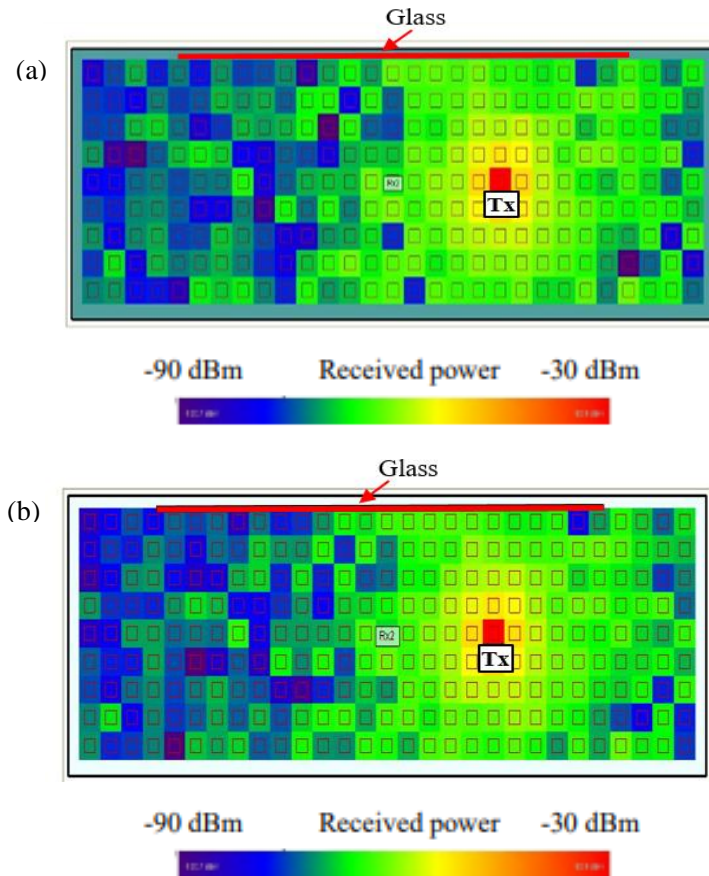
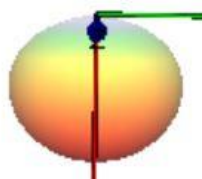


Figure 6.6.2: Simulation results of received power map that employs (a) our material property models, and (b) ITU-R material property models, respectively.

We conducted outdoor radio wave propagation simulations using the measured glass complex permittivity. We employed the building data at Shinjuku area in Japan. In 6G systems, remote antenna units (RAUs) are considered to be mounted on street light and traffic lights at a height ranging from 2.5 m to 5 m in order to achieve ultra-high data rates and ultra-high density. Figure 6.6.3 shows the simulation model for outdoor radio wave propagation. We set the Tx height to be 5 m and, and Rx to be 1.2 m. The Tx and Rx antennas employ a directional antenna with a half power beam width of 60°. The output power of the Tx is 30 dBm.

Figure 6.6.4 shows the received power map in Shinjuku. The walls of the buildings were set to be the heat-absorbing glass, and the complex dielectric constant of the heat-absorbing glass was set to be the value obtained in the experiments shown in Fig. 6.4.5. Judging from the relationship between the receiver sensitivity and the date of the 300-GHz-band wireless link, 33-Gbit/s data transmission can be achieved within a diameter of 4 m.

Antenna pattern



City model

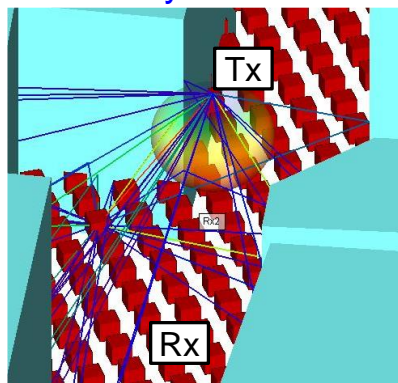


Figure 6.6.3: Simulation model for outdoor radio wave propagation.

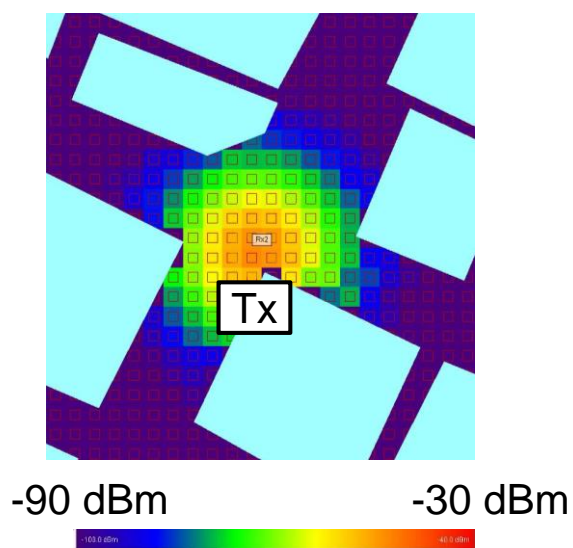


Figure 6.6.4: Received power map in Shinjuku.

7. Conclusion

We have investigated various researches about antenna and propagation models in order to build antenna models and propagation models at 300 GHz.

First, we measured the antenna patterns of low-gain antennas by using a vector network analyser (VNA) and electro-optic (EO) sensor. We measured the far-field radiation patterns of low gain antennas, such as a horn antenna, in an anechoic chamber by using a VNA setup. We also measured the near-field pattern of the low-gain antenna by VNA and EO sensor, and the near-field pattern was transformed to the far-field pattern. The main lobe of the radiation pattern agrees well between the far-field measurement results and the near-field-to-far-field transformation.

We also measured the near-field pattern of a high-gain antenna (Cassegrain antenna) by EO sensor and transformed it to far-field pattern. In order to measure the far-field radiation pattern of Cassegrain antenna, we had conducted trail production of 300-GHz band transmitter for far-field radiation pattern measurement. The transmitter consists of a frequency multiplier. The carrier frequency of the transmitter is 293.4 GHz, and the output power is 1.2 mW. We obtained an experimental radio station licence from Kanto General Communication Bureau on 20th November 2020. The main lobe of the measured far-field pattern of high-gain antenna (Cassegrain antennas) agrees well with the ITU-R models. The side lobes of the measured radiation pattern also agree with the ITU-R models. However, the side lobe of the measurement results become a few dB larger than the ITU-R models at several degrees. In case of the far-field pattern transformed from the near-field pattern measured by EO sensor, the main lobe agrees well with the ITU-R models.

As for the propagation model, we investigated the effects of wind, and found that the probability of gain degradation significant for the 0.6 m-antenna, however the probability of gain degradation can be reduced by 3 dB for the 0.3 m-antenna under the wind condition of 10m/s. We evaluated the diffraction characteristics of THz waves by using the 300-GHz-band Tx/Rx, and compared the measured results with the radio wave propagation simulation. The diffraction loss by 90-degree angled edge is about 30 dB for a y-axis shift larger than 30 cm. The diffraction loss by the obstacle without knife-edge structure becomes 20 dB larger than that with a knife-edge structure.

We measured the complex dielectric constant of building materials, such as glass, concrete, and etc. by VNA and THz-time-domain spectroscopy (TDS). The glass permittivity measured by THz-TDS and VNA was almost the same, and both of the real part and the imaginary part of the complex permittivity was almost constant at 200-500 GHz, and the glass surface roughness of 3-10 μm does not affect the complex permittivity measurement. We used these values for the propagation simulation in metropolitan area. the reflection by building materials, and the dependence of the path loss on weather conditions.

We conducted pass loss investigation to design THz links which offer stable data transmission under various weather conditions, including heavy rain, strong storm, etc., and found that 300GHz THz links can offer over 300m transmission under very severe weather conditions, where the transmission data rate would be close to 100Gb/s using QPSK with 51.84GHz bandwidth (BW).